

Article

Geochemical Study of Cretaceous Magmatic Rocks and Related Ores of the Hucunnan Cu–Mo Deposit: Implications for Petrogenesis and Poly-Metal Mineralization in the Tongling Ore-Cluster Region

Ke Shi ^{1,2,3}, Xiaoyong Yang ^{1,*}, Jianguo Du ^{2,3}, Jingya Cao ¹ , Qiu Wan ^{2,3} and Yang Cai ^{2,3}

¹ CAS Key Laboratory of Crust-Mantle Materials and Environments, University of Science and Technology of China, Hefei 230026, China; shike890815@163.com (K.S.); jingyacao@126.com (J.C.)

² Geological Survey of Anhui Province, Hefei 230001, China; ahdujianguo@126.com (J.D.); att3955@163.com (Q.W.); youngtsai@outlook.com (Y.C.)

³ The Coverage Area Deep Resource Exploration Engineering Technology, Innovation Center of Ministry of Natural Resources, Hefei 230001, China

* Correspondence: xyyang@ustc.edu.cn; Tel.: +86-0551-6465-2201

Received: 23 December 2019; Accepted: 24 January 2020; Published: 26 January 2020



Abstract: The Hucunnan porphyry- and skarn-type Cu–Mo deposit is located in the south of the central Shizishan ore field of the Tongling ore-cluster region. The intrusive Hucunnan granodiorite, outcropping in this deposit, has adakitic geochemical features, and its magma is proposed to have originated from partial melting of the oceanic crust mixed with mantle-derived materials. The porphyry-type orebody is hosted in the granodiorite, whereas the skarn-type orebody occurs in the contact zones of intrusions and country rocks. The $\delta^{34}\text{S}$ values of pyrite from the skarn orebodies ranged from +3.9 to +4.7‰ (avg. +4.3‰, $n = 6$), while those of the porphyry orebodies ranged from +5.1 to +6.2‰ (avg. +5.6‰, $n = 4$). $^{208}\text{Pb}/^{204}\text{Pb}$, $^{207}\text{Pb}/^{204}\text{Pb}$, and $^{206}\text{Pb}/^{204}\text{Pb}$ ratios of the pyrites from the skarn orebodies were 38.04–38.45 (avg. 38.26), 15.55–15.66 (avg. 15.59), and 18.16–18.54 (avg. 18.44), respectively ($n = 6$). The pyrites in the porphyry orebodies had $^{208}\text{Pb}/^{204}\text{Pb}$, $^{207}\text{Pb}/^{204}\text{Pb}$, and $^{206}\text{Pb}/^{204}\text{Pb}$ ratios of 38.24–38.36, 15.51–15.662, and 18.10–18.41, respectively (avg. 38.32, 15.58, 18.22; $n = 4$), respectively. The metallogenic model ages from Re–Os isotopic dating were 138.7 ± 1.9 and 140.0 ± 2.8 Ma, respectively. Geochemical data indicate that the ore-forming fluids in the skarn stage are characterized by high temperature, low acidity, and high oxygen fugacity, and the ore-forming materials were mainly from magma and partly from stratum, proving that the skarn orebody has more stratum materials than the porphyry orebody.

Keywords: EMPA; S–Pb isotopes; Re–Os isotopic dating; metallogenic model; Hucunnan Cu–Mo deposit; Tongling ore-cluster region

1. Introduction

Porphyry and skarn deposits are widely distributed in the world and represent the most important source of Cu, W, Fe, Mo, Pb–Zn, etc. Various petrogenetic and metallogenic models that involved porphyry and skarn deposits have been proposed over the past few decades [1–7]. Porphyry-skarn metallogenesis is a dynamic process, and the development of deposits depends on parameters such as the host rock types, geochemistry of the causative intrusions, and local tectonic history. These deposits can form in either convergent arc systems (island arcs or continental arcs) or collisional settings and they are closely related to intermediate to acidic intrusions [8,9]. With the development of adakite

rocks, some scholars believe that the high oxygen fugacity of adakite magma is closely related to porphyry copper deposits [10].

The Middle-Lower Yangtze River Belt (MLYRB) is a well-known metallogenic belt in eastern China that contains more than 200 polymetallic Cu–Fe–Au–Mo deposits. It hosts seven large-scale ore-cluster regions from northeast to southwest: Ningzhen (Cu, Fe, Pb, Zn), Ningwu (Fe), Tongling (Cu, Au, Pb, Zn), Luzong (Fe, Cu), Anqing-Guichi (Cu, Fe), Jiurui (Cu, Au), and E’dong (Fe, Cu) [11–18]. Among them, the Tongling ore-cluster region has high economic value with a high degree of geological exploration and intense studies ([19–29]; Figure 1a), and it is the birthplace of the theory of “stratabound skarn deposit” [11]. Skarn ore deposits are one of the most important ore types in the Tongling ore-cluster region, and the geochronological, geochemical, and fluid evolution features of this type have been reported in numerous studies [30–32]. However, in recent years, porphyry ore bodies were found in the depth, and there have been relatively few studies on the mineralization of porphyry-skarn type deposits in this area [33–35].

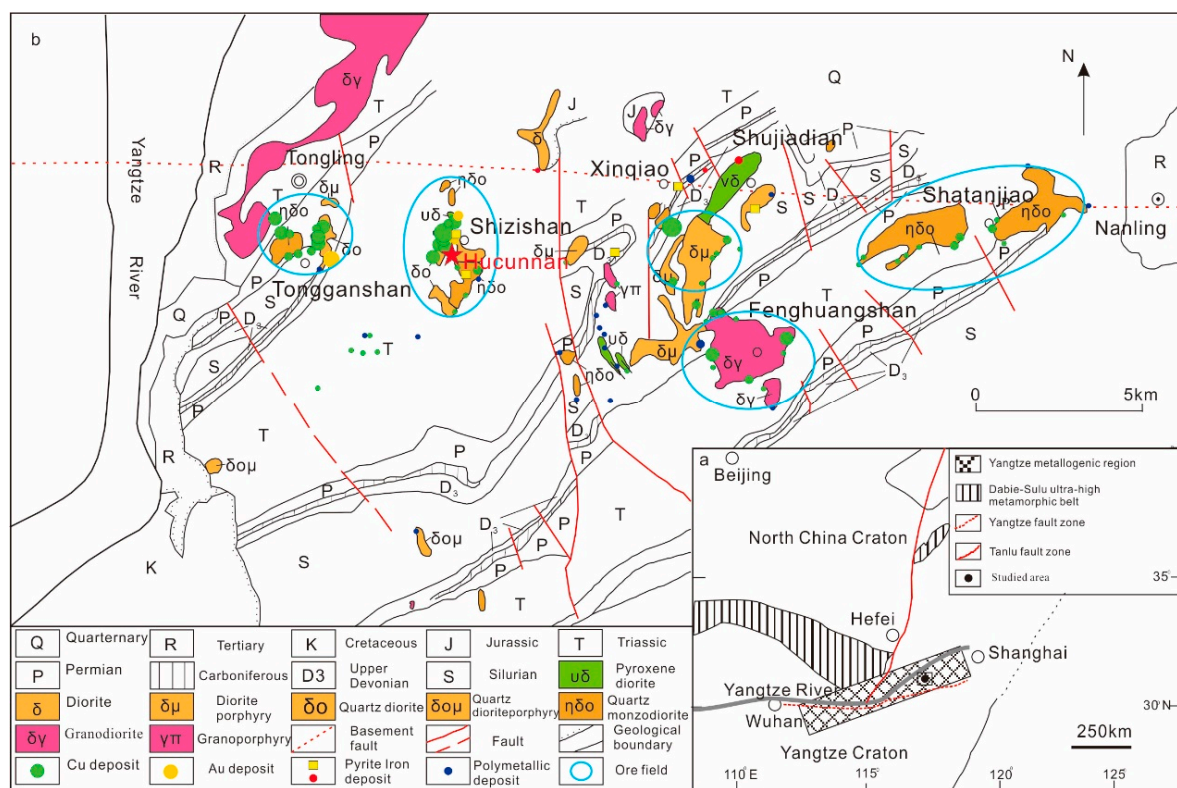


Figure 1. Geological sketch maps of (a) Lower Yangtze River Metallogenic Belt and (b) Tongling ore cluster, East China [26].

As typical porphyry-skarn Cu–Mo polymetallic deposits, the Hucunanan deposit in the Tongling ore-cluster region provides a good example for revealing the magmatic evolution and enrichment and migration of metallogenic materials during the skarn formation process. Previous studies held that the ages of quartz diorites and granodiorite of Hucunanan deposit are 125 Ma and 137.5 Ma, respectively [36]. The H–O isotopic signatures and the study of fluid inclusions show that the ore-forming fluids were dominated by magmatic water in the early stages, and gradually mixed with circulating meteoric water in the late stages [37]. However, there is still a lack of research on the magmatic evolution and source of ore-forming materials.

This study systematically investigated the age, physical conditions (temperature, pressure, and oxygen fugacity), source of mineralization, and petrogenesis of the intrusive rocks in the Hucunanan deposit. Here, the geochemical characteristics of intrusive rock were summarized and the evolution and

source of magma were discussed. We also discussed the S–Pb isotopic compositions of metallic sulfides and the elemental compositions of pyrite and garnet. They can be used to trace the evolution of the environment and the source of ore-forming materials, and play important roles in judging the physical and chemical conditions of ore-forming hydrothermal solution and determining the genetic types of ore deposits [38–41]. The new data provide evidence related to the evolutionary history of ore-forming hydrothermal system, all of which are necessary for understanding the ore-forming process.

2. Geological Setting

The Tongling ore-cluster region is along the lower Yangtze depression in the northern Yangtze block and belongs to the secondary uplift depression, which is also known as the Tongling uplift [11]. Apart from the absence of Lower and Middle Devonian strata, the main stratigraphic system of this region is from Silurian to Triassic (Figure 1b) [42]. The Cu–Au orebodies are mainly located in neritic-facies and littoral-facies carbonate sequences, e.g., the Carboniferous Huanglong and Chuanshan Formations and the Lower Permian Nanlinghu Formation. There are more than 70 magmatic plutons in the Tongling ore-cluster region. They are distributed from east to west for nearly 25 km in the Tongling–Daijiahui magmatic belt (Figure 1b). These magmatic rocks are divided into four rock assemblages [43,44]: (1) Pyroxene diorite–pyroxene monzodiorite combination, (2) quartz diorite–quartz monzodiorite combination, (3) granodiorite combination, and (4) K-feldspar granite. The ages of granodiorites are concentrated in the range of 144–137 Ma, whereas pyroxene diorite–pyroxene monzodiorite and quartz diorite–quartz monzodiorite range from 143–137 Ma and 140–136 Ma, respectively [19]. The quartz monzodiorite and granodiorite are closely related to copper mineralization, and belong to high potassium calc–alkaline and olivine anorthite [25]. There are three groups of faults in the basement of the Tongling ore-cluster region with trending directions of EW, SN, and N–NE. In addition, there are three groups of shallow fault systems, i.e., NE, NS, and NW. These structures controlled the distribution of rocks and deposits in this area.

There are more than 200 ore deposits in the Tongling ore-cluster region, which are divided into five ore fields: Tongguanshan (Cu, Au, Fe), Shizishan (Cu, Au, S, Pb, Zn), Xinqiao–Shujiadian (Cu, S, Au), Fenghuangshan (Cu, Au, Fe), and Shatanjiao (Pb, Zn, Au, Cu) (Figure 1b) [11]. The metallogenic age gradually changes from east to west, the metallogenic age difference of the adjacent ore fields is about 2 Ma, and the metallogenic ages of the whole ore-cluster region are between 141 and 137 Ma [19]. According to different mineralization, the deposits in the area can be divided into porphyry, sedimentation-hydrothermal superposition reworked type, skarn, hydrothermal, and weathering types (Table 1).

Table 1. Classification of metal ore deposits in the Tongling ore-cluster region.

Type	Subgenera	Mineralization	Example Deposits
Skarn	Contact metasomatism type	Cu, Cu–Fe, Au–Cu, Cu–Mo, Mo	Fenghuashan, Yaoyuanshan, Bishan
	Stratified skarn type	Cu–S, Cu, S–Cu–Au, Au–As–S	Dongguashan, Xinqiao, Tongshan, Tianmashan
	Ore magma type	Cu–Au, Cu–Fe	Dongshizishan
Hydrothermal		Pb, Zn–Au–Cu, Au–Cu, Pb, Zn	Yaojiali, Baimangshan, Caoshan, Cishan
Porphyry		Cu, Cu–Au, Cu–Mo	Shujiadia, deep of Donggushan, Hucunann
Sedimentation-hydrothermal superposition reworked type		S–Au, S–Fe, Fe	Simenkou
Gossan		Au–Fe	Ji Guan Shan
Laterite		Au	Long Tan Xiao

3. Geology of Deposit

The Hucunnan Cu–Mo deposit, a medium-sized porphyry- and skarn-type deposit, is located in the south of Shizishan orefield in the Tongling ore-cluster region (Figure 1b). The exposed surface strata, exposed in the mining area, are mainly Middle Triassic Dongmaanshan Formation (T_2d) limestone and dolomite (Figure 2a), and the deep part is Early Triassic (T_1) and Permian (P) sedimentary rocks.

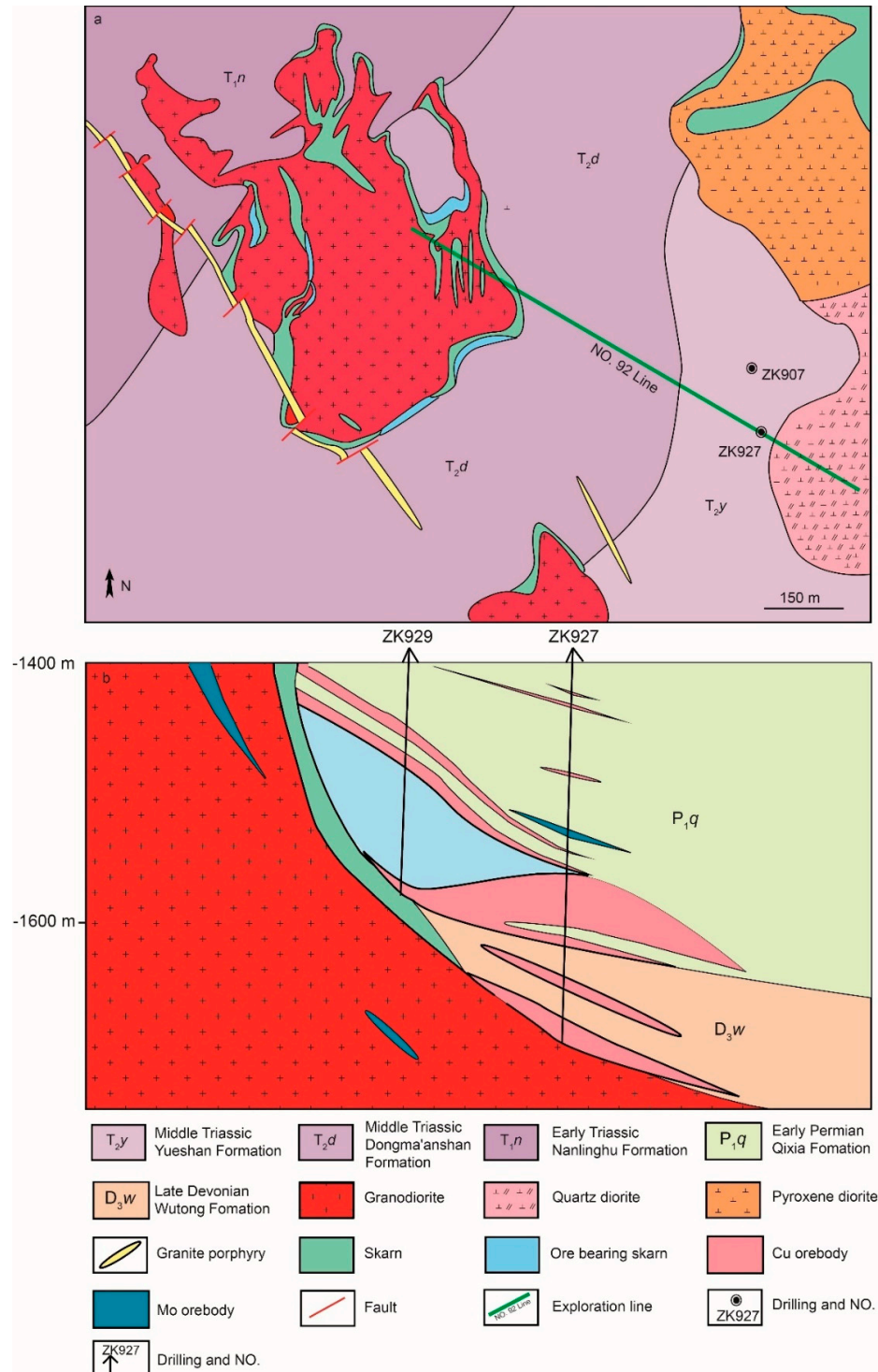


Figure 2. (a) Modified geological sketch map of Hucunnan area; (b) drilling geological profile of Hucunnan Cu–Mo deposit [45].

The fold structures in the mining area are Qingshanjiao anticline and Zhucun syncline. The main faults can be classified into three groups, i.e., SN, NW–W, and N–NE directions, which are important rock- and ore-controlling structures in this area.

The most important intrusive rock of this deposit is Hucun pluton, which is composed of granodiorite (Figure 3a). The granodiorite is light gray and the major minerals are quartz (25%), plagioclase (45%), K-feldspar (20%), amphibole (6%), and biotite (4%) (Figure 3b,c).

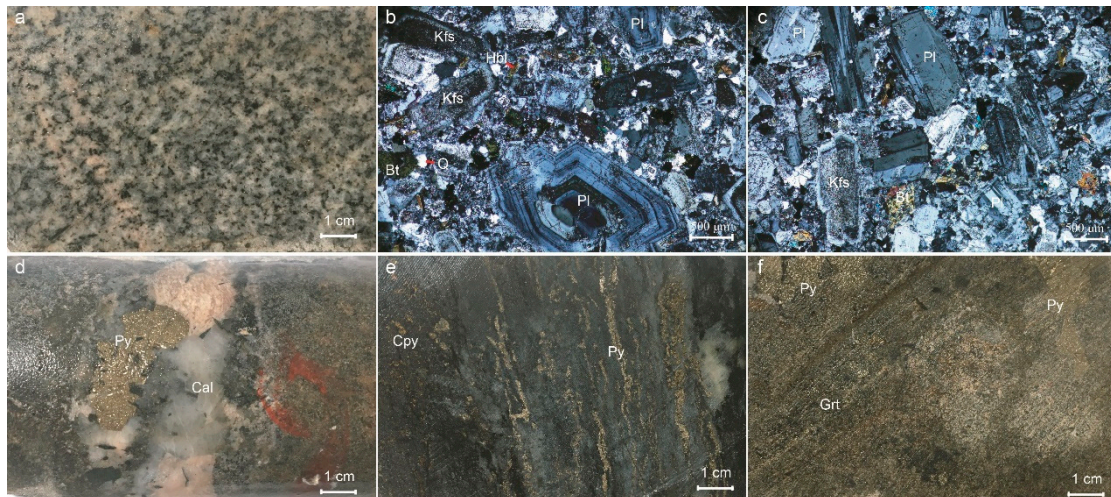


Figure 3. Hand specimens and photomicrographs of rock and mineralogy in the Hucun Cu–Mo deposit. (a) Granodiorite hand specimen; (b,c) granodiorite photomicrograph; (d) granular pyrite; (e) vein pyrite; (f) pyrite in skarn. Py, pyrite; Cpy, chalcopyrite; Kfs, K-feldspar; Bt, biotite; Q, quartz; Pl, plagioclase; Hbl, hornblende; Grt, garnet; Cal, calcite.

There are two types of orebodies in the Hucun deposit, i.e., skarn and porphyry type. The porphyry-type orebody is located in the granodiorite, and the skarn-type orebody is located in the contacts of intrusions and country rocks (Qixia and Gufeng Formation) (Figure 2b). The Cu mineralization is dominant in the adjacent contact zones of the southwest and northeast sides of the intrusion. Generally, the orebodies strike N 30° and dip 10°–25° to the southeast. The Cu orebody is 6.30–19.40-m thick, with an average grade of 0.54–0.69%. Mo mineralization is dominant in the interior of the NE-trending intrusion. The maximum thickness of Mo orebody is 116.71 m, with an average grade of 0.069–0.107%.

Metal minerals are mainly chalcopyrite, pyrite, and molybdenite, followed by magnetite, sphalerite, and galena. Gangue minerals are mainly quartz, garnet, pyroxene, calcite, plagioclase, and potassium feldspar, followed by biotite, sericite, epidote, and chlorite. The ore structure is diverse, including automorphic–semi-automorphic, heteromorphic, metasomatic, and solid solution separation structures. The structures are mainly disseminated, veined, and reticulated (Figure 3d–f).

Field evidence, petrographic observations, and cross-cutting and replacement relationships indicate that hydrothermal activity occurred in four stages during the formation of the Hucun deposit: (1) Skarn stage, (2) oxide stage, (3) quartz–sulfide stage, and (4) quartz–carbonate stage (Table 2).

The garnets were usually reddish brown, with mainly rhombic dodecahedron or tetragonal trihedron self-shaped/semi-self-shaped granular structures. The particle size was generally 3–6 mm, with a small part reaching more than 1 cm, and the band structure was obvious. The pyrites were usually bright yellow, automorphic/semi-automorphic, disseminated, and reticulated.

4.2. Analysis

4.2.1. Whole-Rock Major and Trace Elements

Whole-rock major and trace elements of fresh samples were analyzed by ALS Minerals–ALS Chemex (Guangzhou, China).

Major elements were determined by ME-XRF26 spectrometry. A prepared sample was fused with lithium metaborate–lithium tetraborate flux, which also included an oxidizing agent (lithium nitrate), and then poured into a platinum mold. The resultant glass disk was analyzed by X-ray fluorescence (XRF) spectrometry. The XRF analysis was determined in conjunction with a loss-on-ignition at 1000 °C. The resulting data from both determinations were combined to produce a total.

Trace elements and rare earth elements (REE) were determined by inductively coupled plasma-mass spectrometry (ICP-MS) and inductively coupled plasma-atomic emission spectroscopy (ICP-AES). First, we prepared two pulp subsamples. One subsample was digested with perchloric, nitric, and hydrofluoric acids. The residue was leached with diluted hydrochloric acid and diluted to volume. The solution was then analyzed by ICP-MS for ultra-trace-level elements. The same digestion solution was also analyzed by ICP-AES for trace-level elements. Results were corrected for spectral interelement interference. The other subsample was added to lithium metaborate/lithium tetraborate flux, mixed well, and fused in a furnace at 1025 °C. The resulting melt was then cooled and dissolved in an acid mixture containing nitric, hydrochloric, and hydrofluoric acids. This solution was then analyzed by ICP-MS. According to the actual situation of the sample and the digestion effect, the comprehensive value was the final test result.

4.2.2. EPMA

The element composition of pyrite was determined using a JEOL JXA-8230M electron microprobe at the School of Resources and Environmental Engineering, Hefei University of Technology, Hefei, China. The analytical conditions were as follows: Accelerating voltage of 15 kV, probe current of 20 nA, and peak diameter of 5 µm.

4.2.3. Sulfur Isotope

The S isotope was tested at the Chinese Academy of Geological Sciences, Beijing, China. Samples contained no more than 100 µg of sulfur and three to five times the amount of V₂O₅, wrapped in 9-mm × 5-mm tin cups. They were automatically sampled in the combustion reactor with an oxygen supply and sufficient combustion under 1020 °C. All gas was combusted under helium load flow into and through the WO₃ filler and redox reaction of Cu wire tube, and all gas was oxidized adequately. At the same time, a small amount of SO₃ was generated through the reduction of SO₂ by the Cu wire. Gas was separated from SO₂ and other impure gases by a column (PN 260 070 80 Sulphur Separation Column for IRMS/HT) and then tested by mass spectrometry. Three international standard substances, IAEA-SO-5, IAEA-SO-6, and NBS 127, were used. The accuracy of standard sample analysis was better than 0.2‰.

4.2.4. Pb Isotope

The Pb isotope was tested at the Chinese Academy of Geological Sciences, Beijing, China. For determination of Pb isotope composition, all the methods were static. ²⁰²Hg⁺ was measured to monitor the interference of ²⁰⁴Hg⁺ to ²⁰⁴Pb⁺ in argon. ²⁰⁵Tl⁺ and ²⁰³Tl⁺ were measured to use ²⁰³Tl/²⁰⁵Tl as an external standard calibration instrument for mass fractionation effect. Before testing

the samples, the parameters of Neptune Plus were optimized using NIST 981 200 ug/L standard solution, including plasma parameters (rectangular tube position and carrier gas velocity) and ion lens parameters, in order to achieve maximum sensitivity. The sample after chemical separation underwent mass spectrometry with 2% HNO₃ solution, and the signal intensity of ²⁰⁸Pb⁺ was about 8 V (the concentration of Pb in solution was about 200 ug/L). The sample was injected by free atomizer. The lead isotope ratio was normalized by ²⁰³Tl/²⁰⁵Tl = 0.418922.

4.2.5. Re–Os Isotope

The Re–Os isotope analysis of molybdenite was completed at the Chinese Academy of Geological Sciences, Beijing, China. The isotope dilution Carius tube reverse water sample technique was used to seal and melt the sample for 24 h at 220 °C [46], direct distillation was used to separate and enrich Os [47], acetone extraction was used to separate and purify Re [48], and four-stage rod mass spectrometry (thermoelectric company x-series) was used to determine isotope ratios.

5. Results

5.1. Whole-Rock Geochemistry

The major and trace element results are listed in Supplementary Materials Table S1 and plotted in Figures 4 and 5, respectively.

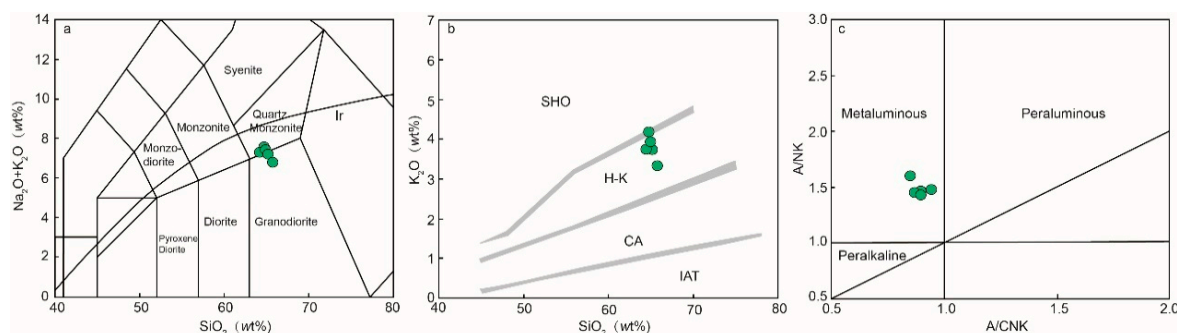


Figure 5. Classification diagrams of lithochemical compositions of Hucunnan granodiorites: (a) Total alkali vs. silica (TAS) [49]; (b) K₂O–SiO₂ [50]; (c) A/NK vs. A/CNK [51]. Ir—The Irvine dividing line, the top is alkaline, and the bottom is sub-alkaline; SHO—Potassium basalt series; H-K—High potassium calcium basic series; CA—Calc-alkaline series; IAT—Low potassium series.

The Hucunnan samples (SiO₂, 64.49–65.77 wt.%) are granodiorites, based on geochemistry (Figure 5a). The total alkali contents (Na₂O + K₂O) mainly ranged from 6.77 wt.% to 7.47 wt.%, of which K₂O contents ranged from 3.34 wt.% to 4.17 wt.% and Al₂O₃ contents from 14.45 wt.% to 15.50 wt.%. They are mostly plotted in the field of high-K calc-alkaline series on the SiO₂ versus K₂O diagram (Figure 5b). The alkali-aluminum ratios A/NK = Al₂O₃/(K₂O + Na₂O) ranged from 1.43 to 1.59, and aluminum saturations A/CNK = Al₂O₃/(CaO + K₂O + Na₂O) ranged from 0.85 to 0.95, indicating that they are metaluminous (Figure 5c).

The primitive mantle-normalized trace element distribution patterns (Figure 6a) show that large ion lithophile elements (LILEs) Rb (121.5–159.5 ppm), Ba (858–1010 ppm), Sr (657–727 ppm), and Th (8.68–10.05) were enriched, and there was a deficit of high-field strong elements (HFSEs) Nb (12.0–12.8 ppm), Y (14.5–16.4 ppm), and Yb (1.36–1.69 ppm). REE was 131.66–157.48 ppm, light rare earth elements (LREE)/HREE were between 11.93–12.99, and the chondrite-normalized REE pattern was right-inclined (Figure 6b). (La/Yb)_n was 16.14–19.57, indicating a high degree of fractional distillation of HREE and LREE in this intrusion.

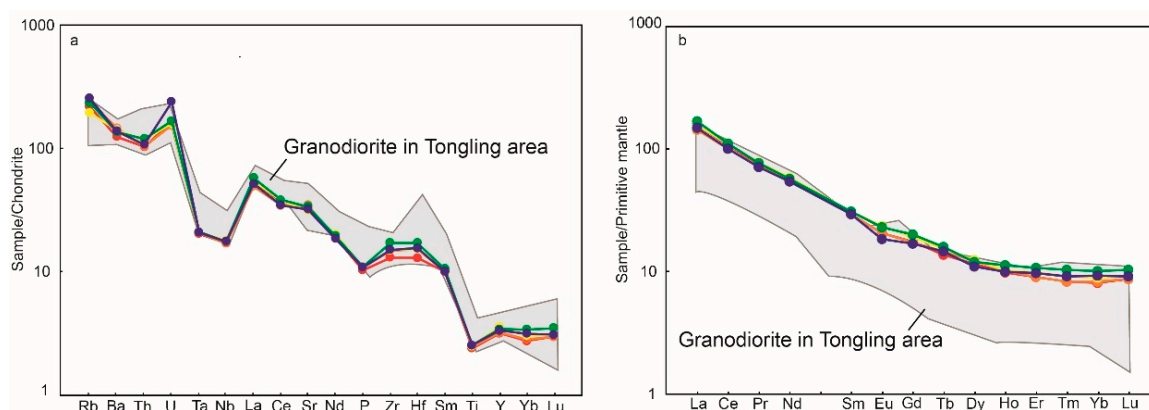


Figure 6. (a) Primitive mantle-normalized trace element variation; (b) chondrite-normalized rare earth element pattern. Data are taken from [52].

5.2. Mineral Geochemistry

5.2.1. Biotite Composition

The EPMA result of the biotite is listed in Supplementary Materials Table S2.

Biotites of the Hucunna granodiorite belong to magnesia biotite series (Figure 7). SiO_2 content ranged from 36.95 wt.% to 39.85 wt.%, FeO from 13.71 wt.% to 16.88 wt.%, MgO from 13.22 wt.% to 15.87 wt.%, and Al_2O_3 from 12.20 wt.% to 13.79 wt.%.

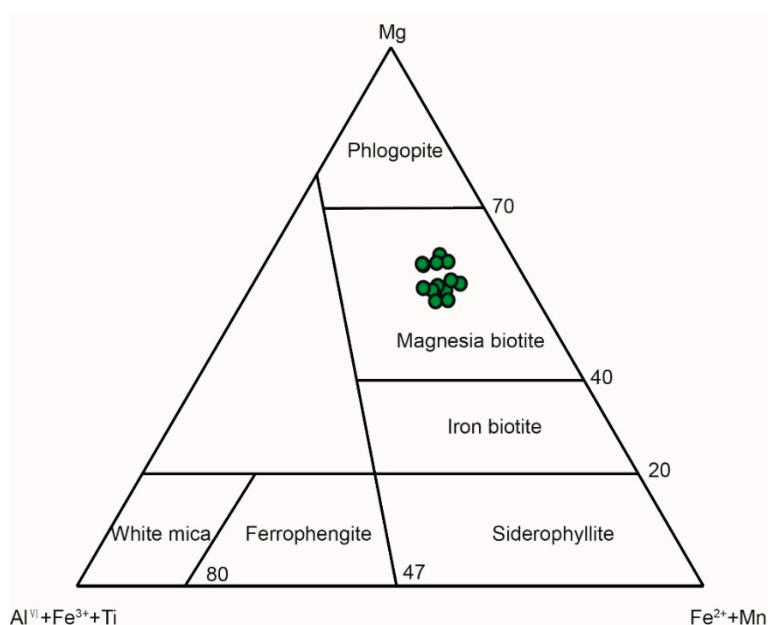


Figure 7. Biotite classification map [53].

5.2.2. Garnet Composition

The EPMA results of the garnet are listed in Supplementary Materials Table S3.

The individual garnets had high SiO_2 and CaO contents: SiO_2 contents were 32.45–36.38 wt.% (avg. 35.26 wt.%, $n = 17$) and CaO contents were 29.45–33.58 wt.% (avg. 32.61 wt.%, $n = 17$). FeO contents were 17.23–27.42 wt.% (avg. 24.91 wt.%, $n = 17$). Al_2O_3 contents were 0.07–7.20 wt.% (avg. 24.91 wt.%, $n = 17$). The contents of TiO_2 , Cr_2O_3 , MnO, and MgO were relatively low, i.e., 0.00–0.14 wt.% (avg. 0.04 wt.%, $n = 17$), 0.00–0.24 wt.% (avg. 0.03 wt.%, $n = 17$), 0.18–0.83 wt.% (avg. 0.34 wt.%, $n = 17$), and 0.00–0.33 wt.% (avg. 0.08 wt.%, $n = 17$), respectively.

5.2.3. Pyrite Composition

A total of 17 EPMA spot analyses were completed on pyrite, 10 on Py_{SK} and 7 on Py_{GD} from the Hucunna deposit. The EPMA results of the pyrite are listed in Supplementary Table S4.

Fe contents were 45.95–47.95 wt.% (avg. 47.06 wt.%, $n = 10$) in Py_{SK} samples and 46.72–47.76 wt.% (avg. 47.73 wt.%, $n = 7$) in Py_{GD} samples. S contents were 50.76–53.85 wt.% (avg. 52.11 wt.%, $n = 10$) in Py_{SK} samples and 51.63–54.31 wt.% (avg. 52.78 wt.%, $n = 7$) in Py_{GD} samples. Cu contents were 0.002–0.061 wt.% (avg. 0.034 wt.%, $n = 10$) in Py_{SK} samples and 0.011–0.041 wt.% (avg. 0.026 wt.%, $n = 3$) in Py_{GD} samples.

5.3. Isotope Geochemistry

5.3.1. S Isotope

The S isotope composition of different orebodies types is shown in Supplementary Materials Table S5. Our results show that the $\delta^{34}\text{S}$ values of pyrite from the skarn orebodies ranged from +3.9‰ to +4.7‰ (avg. +4.3‰, $n = 6$), while those of the porphyry orebodies ranged from +5.1‰ to +6.2‰ (avg. +5.6‰, $n = 4$).

The S isotope composition of the different orebody types at Hucunna differed slightly, but the two generally had little change and were close, which indicates that different types of orebodies may have the same S source but were slightly different in the evolution process.

5.3.2. Pb Isotope

The Pb isotope composition of different types of orebodies is shown in Supplementary Table S6. The pyrite in the skarn orebodies had $^{208}\text{Pb}/^{204}\text{Pb}$, $^{207}\text{Pb}/^{204}\text{Pb}$, and $^{206}\text{Pb}/^{204}\text{Pb}$ ratios of 38.04–38.45, 15.55–15.66, and 18.16–18.54 (avg. 38.26, 15.59, 18.44; $n = 6$), respectively. The pyrite in the porphyry orebodies had $^{208}\text{Pb}/^{204}\text{Pb}$, $^{207}\text{Pb}/^{204}\text{Pb}$, and $^{206}\text{Pb}/^{204}\text{Pb}$ ratios of 38.24–38.36, 15.51–15.662, and 18.10–18.41 (avg. 38.32, 15.58, 18.22; $n = 4$), respectively.

The Pb isotope composition of the Hucunna deposit was similar to that of the feldspar of granitoids in the Tongling ore cluster ($^{208}\text{Pb}/^{204}\text{Pb} = 38.090\text{--}38.460$, $^{207}\text{Pb}/^{204}\text{Pb} = 15.470\text{--}15.600$, $^{206}\text{Pb}/^{204}\text{Pb} = 17.940\text{--}18.420$) (Tang et al., 1998, [42]), which indicates that the Hucunna deposit and the intermediate-felsic intrusions in Tongling may have shared a similar Pb source.

5.3.3. Re–Os Isotope Dating

The results of Re–Os isotope are listed in Supplementary Materials Table S7. The content of ^{187}Re was 8686.80 and 17863.42, and ^{187}Os was 20.28 and 41.33. Both of them changed greatly. The metallogenic ages of Hucunna Cu–Mo deposit are 138.70 ± 1.87 and 140.03 ± 2.8 Ma, from Late Jurassic to Early Cretaceous.

6. Discussion

6.1. Petrogenesis of the Hucunna Granodiorite

The granodiorite of the Hucunna Cu–Mo deposit is consistent with the magmatic rock related to copper ore in the Shizishan ore field, both of which belong to the high-K calcium alkaline series.

The chemical compositions of biotite can also reflect oxidation conditions during magma crystallization. The concentrations of Fe^{3+} , Fe^{2+} , and Mg^{2+} in biotite, which is paragenetic with K-feldspar and magnetite, can be used to calculate magmatic oxygen fugacity [54–58]. From the Fe^{3+} – Fe^{2+} – Mg diagram of biotite in the intrusion (Figure 8a), it can be seen that the sample points of biotites fall between the two buffer lines of Ni–NiO and Fe_2O_3 – Fe_3O_4 , indicating that biotite was crystallized under the condition of high oxygen fugacity [57]. The contents of MgO and FeO in biotite can determine the source of magmatic material. In the MgO – $\text{FeO}/(\text{FeO} + \text{MgO})$ diagram for biotites

(Figure 8b), data are mainly plotted in the crust–mantle mixed-source area, indicating that Hucunnan granodiorite has the characteristics of crust–mantle mixed source.

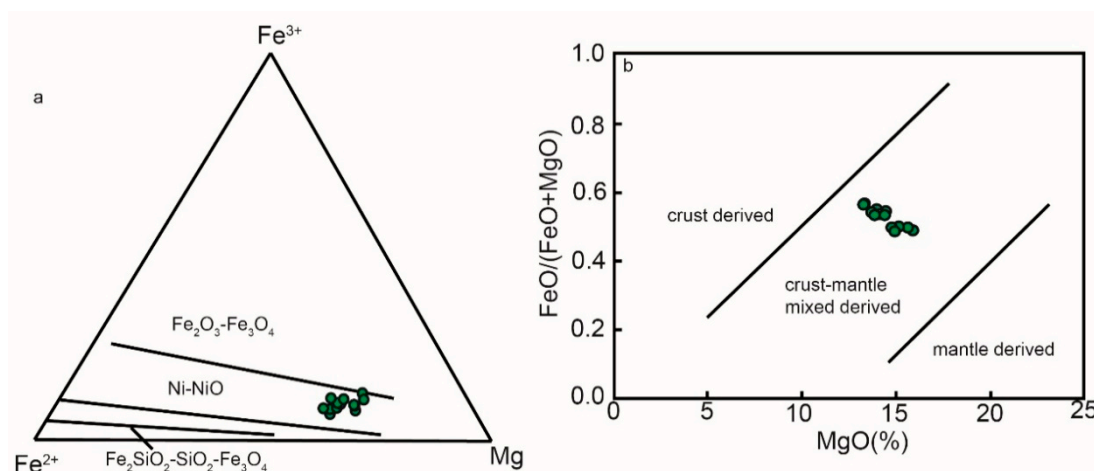


Figure 8. (a) Fe^{3+} – Fe^{2+} – Mg [58], and (b) $\text{FeO}/(\text{FeO} + \text{MgO})$ vs. MgO for biotites from Hucunnan granodiorite [59].

The Hucunnan granodiorite was enriched in K, Al, and Na; enriched in large ion lithophile and light rare earth elements; depleted in high-field-strength elements Nb, Ta, and Ti; and obviously enriched in Sr and Ba, but Rb was low. The Rb/Y – Nb/Y diagram (Figure 9a) shows that the distribution of Hucunnan granodiorite was basically along the line of the evolution of crustal contamination or subduction zones. These characteristics reflect that the original magma came from the lithospheric mantle, and the lithospheric mantle source area may have been caused by plate subduction and may also reflect crust mixing during the magma rising process.

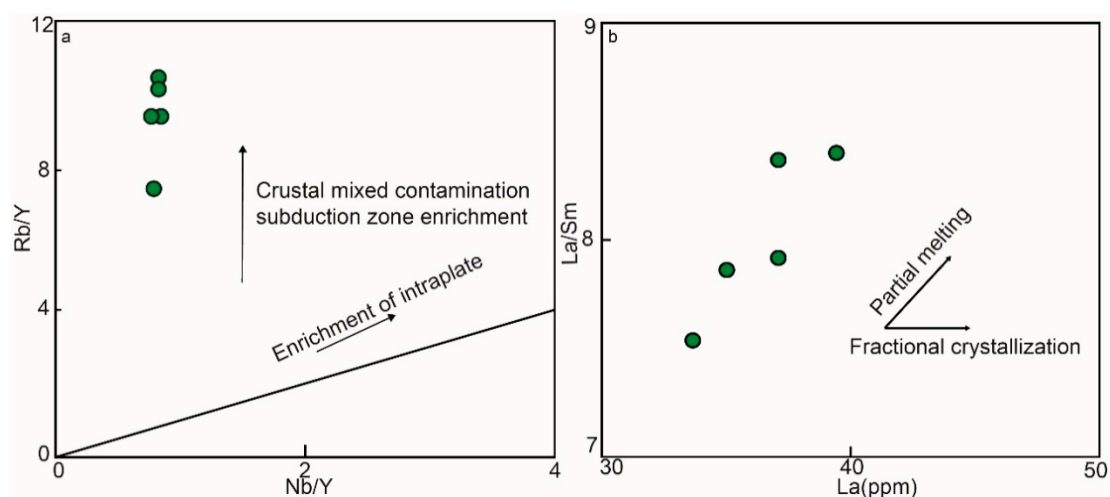


Figure 9. (a) Rb/Y – Nb/Y and (b) La/Sm – La for Hucunnan granodiorite.

In the La/Sm – La diagram (Figure 9b), the La/Sm ratio and La content of the sample show an obvious linear increasing trend on the partial melting evolution line, indicating that partial melting occurred in the process of magma evolution. In the Harker diagram (Figure 10), Al_2O_3 , CaO, P_2O_5 , TiO_2 , and MgO decreased with the increase of SiO_2 , indicating that with the evolution of magma, hornblende, pyroxene, sphene, biotite, and other minerals in the magma gradually underwent precipitation crystallization separation, and crystallization differentiation occurred during the evolution of magma. However, Na_2O , did not change with SiO_2 .

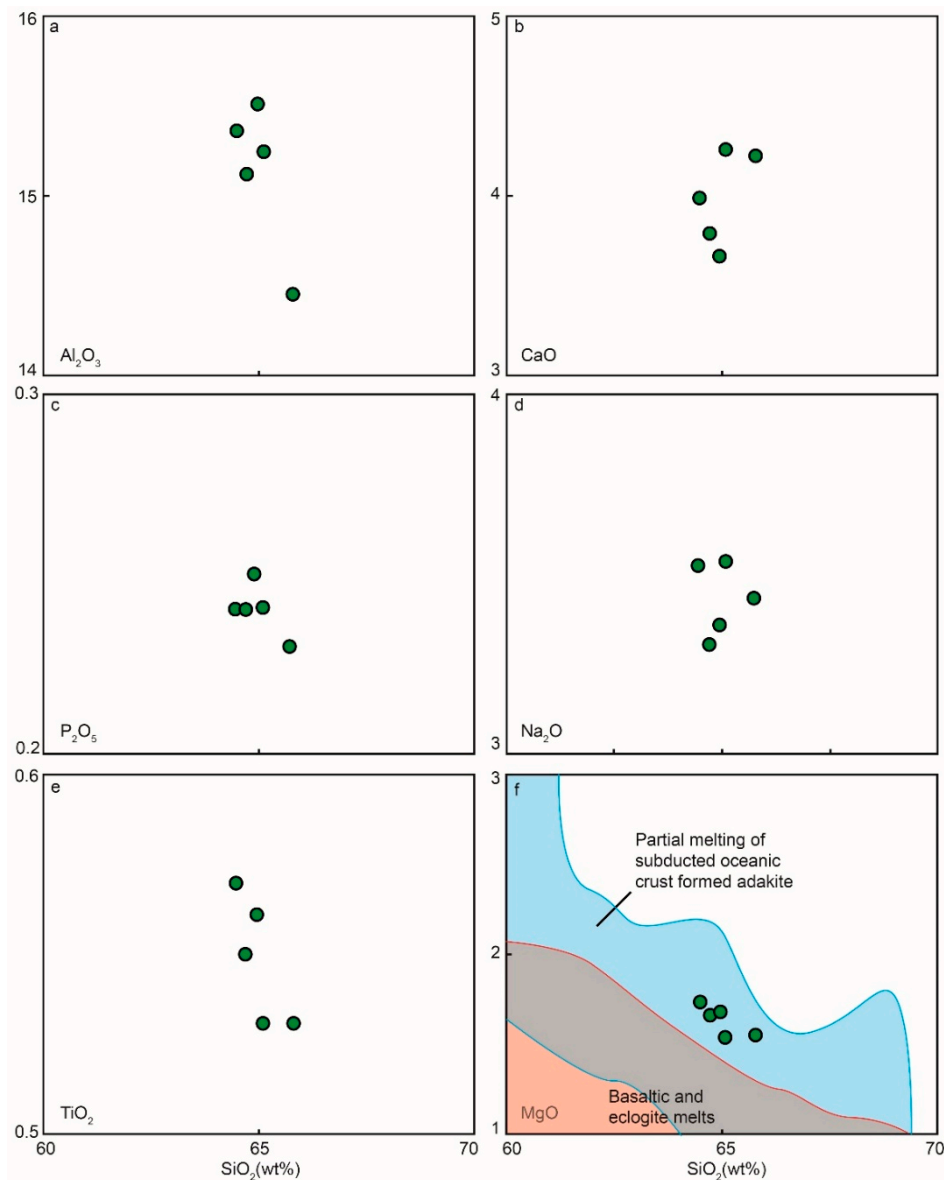


Figure 10. Harker diagram of SiO_2 versus other major elements of Hucunnan granodiorite: (a) SiO_2 vs. Al_2O_3 , (b) SiO_2 vs. CaO , (c) SiO_2 vs. P_2O_5 , (d) SiO_2 vs. Na_2O , (e) SiO_2 vs. TiO_2 , (f) SiO_2 vs. MgO .

MgO and SiO_2 of granodiorite in the area were negatively correlated, reflecting the typical characteristics of subducted oceanic crust melting adakite (Figure 10f) [60]. In the Sr/Y - Y diagram (Figure 11a), all samples show a negative correlation trend and fall within the area of adakite with an affinity of melting of oceanic subduction, which is obviously different from that of melting of thickened lower continental crust (Figure 11b).

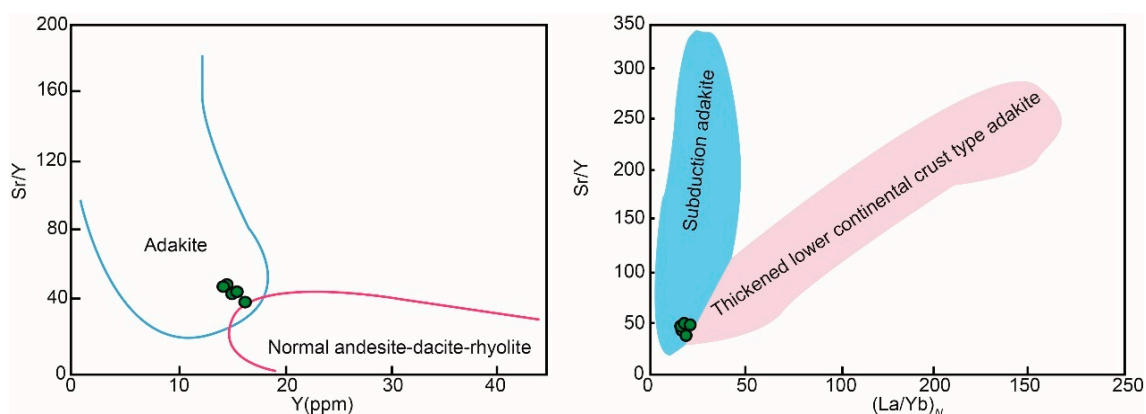


Figure 11. (a) Sr/Y - Y and (b) Sr/Y - $(La/Yb)_N$ for Hucunnan granodiorite [61].

To sum up, we believe that the Hucunnan granodiorite is adakite that originated from the partial melting of oceanic crust, mixed with mantle-derived materials. After melting, the magma underwent crystallization differentiation of hornblende, pyroxene, sphene, biotite, and other minerals, and the crystallization environment had high oxygen fugacity.

6.2. Evolutionary Characteristics of Garnet

Garnet is the main skarn mineral in the Hucunnan deposit. In this study, the main elements of garnet at different locations were measured by electron probe. According to the distance from intrusion, the elements from far to near were zk927-b24, zk907-b59, and zk927-b26, respectively.

As one of the common minerals in skarn-type polymetallic deposits, garnet can be used to indicate the diagenetic and metallogenic process of skarn and serve as a direct indicator of mineralized species and genera [62,63]. In the Hucunnan Cu–Mo deposit, the end-member compositions were andradite (And = 61.91–97.88%), grossularite (Gro = 1.19–34.16%), spessartite (Spe = 0.43–2.11%), pyrope (Pyr = 0.00–1.53%), and almandine (Alm = 0.00–1.74%), which belong to the series of andradite and grossularite solid solutions. The molecular contents of the andradite are similar to the end components of garnet in skarn-type Cu–Mo deposits in the world (Figure 12a).

As skarn gradually moves away from the contact zone and the influence of alteration, its mineral composition also shows a certain change trend. The contents of andradite and grossularite in the Hucunnan deposit were linearly correlated (Figure 12b), and the composition of garnet gradually changed from andradite to grossularite with the direction close to the intrusion. This indicates that the metasomatism of fluid may have decreased gradually with the change of spatial position. There was a negative correlation between FeO and Al_2O_3 (Figure 12c), and a slight positive correlation between SiO_2 and CaO (Figure 12d). With the increase of Fe content, Al content in garnet decreases obviously, which reflects the variation characteristics of composition in the Ca–Fe–Ca–Al garnet solid–melt system and was formed under nonequilibrium condition [64].

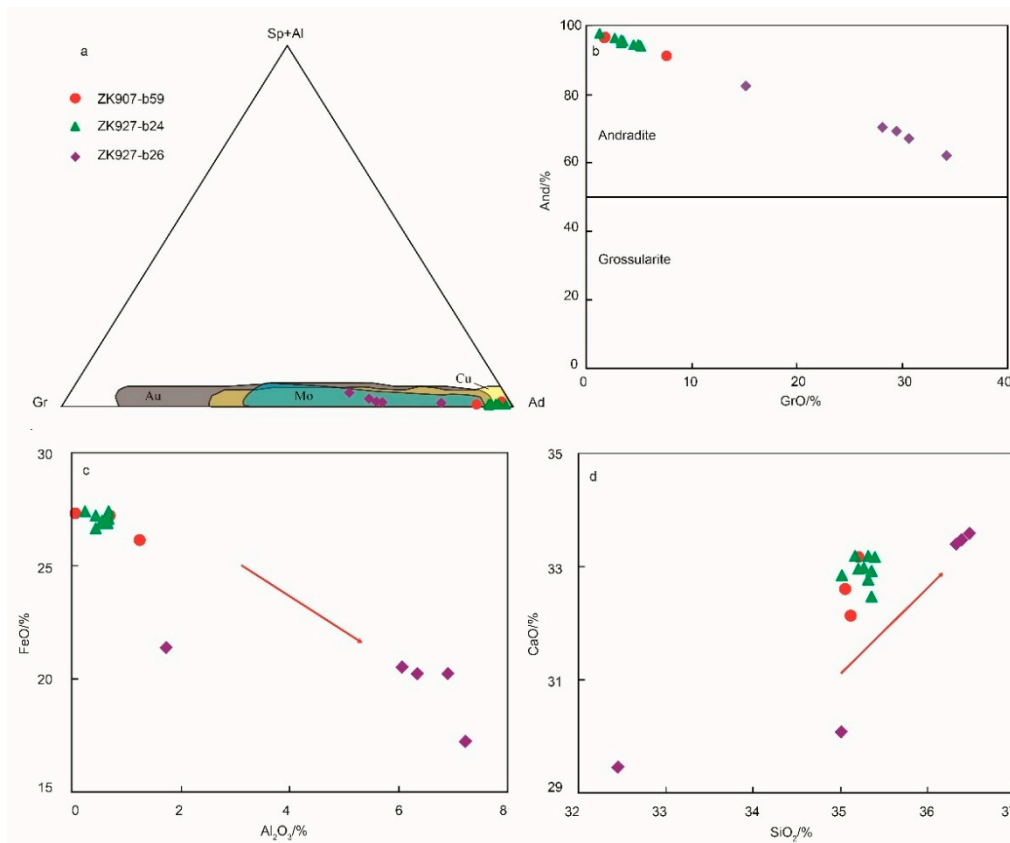


Figure 12. (a) Classification of garnets [65], (b) And–GrO of garnets, (c) Fe₂O₃/Al₂O₃ of garnets, and (d) CaO–SiO₂ of garnets from Hucunna Cu–Mo deposit. And, andradite; Gr, grossularite; Sp, spessartite; Al, almandine.

Skarn mineral composition is closely related to intrusive rock composition, surrounding rock composition, depth, oxygen fugacity, temperature, pressure, etc. [66]. Based on comprehensive research on the main mineral composition and symbiotic combination of skarn in skarn deposits, the changes in physical and chemical conditions in the process of diagenesis and mineralization of the deposit can be revealed. Changes in the mineral compositions of garnet have important indicative significance for the formation environment of skarn [63]. The Fe²⁺/Fe³⁺ ratios of garnet mineral in the Hucunna deposit were 0.00–0.04, indicating that it was formed in an oxidized environment. The end members of the minerals are composed of Gro_{1.19–34.16}And_{61.91–97.88}Spe + Pyr + Alm_{0.62–3.85}, which is dominated by andradite, indicating that it was formed under more oxidized conditions [67]. Previous experiments on the physical and chemical conditions for the formation of andradite showed that its main formation temperature was 450–600 °C, and it was in an oxidation-weak alkaline environment with pH 4.0–11.0 [68], indicating that the ore-forming fluids in the skarn stage of the Hucunna deposit can be characterized by high temperature, low acidity, and high oxygen fugacity.

6.3. Mineralization and Material Source

The metallogenic model ages of the Hucunna Cu–Mo deposit are 138.70 ± 1.87 Ma and 140.03 ± 2.8 Ma, which are consistent with the main metallogenic ages of the Tongling ore-cluster region [19]. The diagenetic age of Hucunna granodiorite measured by predecessors is 137.5 ± 1.2 Ma [36], indicating that the age of diagenesis and mineralization is basically the same. Therefore, the formation of the Hucunna Cu–Mo deposit may be closely related to the Hucunna granodiorite.

Variations of Fe and S contents (Figure 13a) are predominantly related to trace metal substitution in pyrite [69]. The well-defined negative correlation between Cu and Fe in the Hucunna deposit (Figure 13b) indicates Cu²⁺ substitution for Fe²⁺ in pyrite [70]. Previous studies suggested that Cu can

be structurally bound in pyrite, reaching weight percent levels [70,71], and can also be concentrated in pyrite due to micro- or nanoparticle inclusions of chalcopyrite [72]. We propose that the negative correlation of Cu and Fe is due to Cu^{2+} solid solution in pyrite because of the low Cu contents in the studied pyrite samples and pyrite coexisting with chalcopyrite. The elemental compositions of pyrite in skarn type and porphyry type have similar evolutionary trends, indicating that they may have had the same source of ore-forming materials.

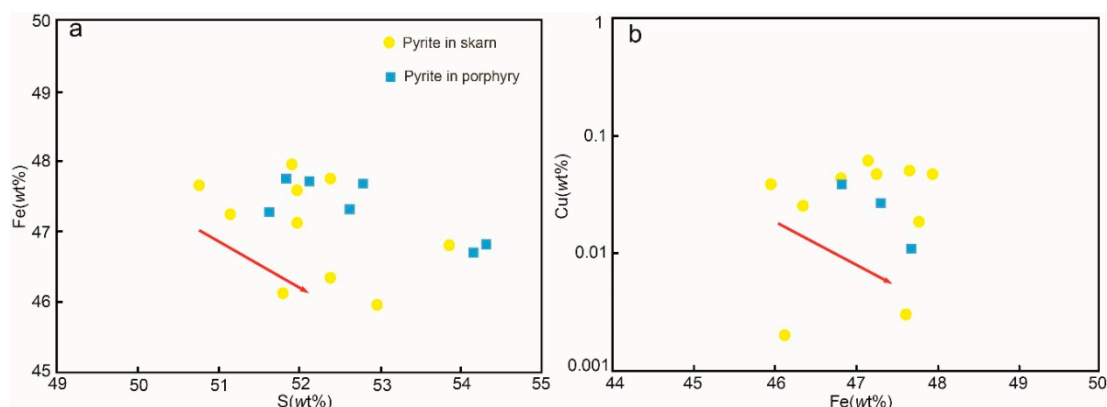


Figure 13. (a) Fe–S and (b) Cu–Fe of pyrites from the Hucunnan Cu–Mo deposit.

The sulfur isotopic composition of metal sulfide is widely used to trace the source of sulfur in ore deposits. $\delta^{34}S$ will vary greatly from one source to another. From mantle sulfur, $\delta^{34}S$ will be $0 \pm 3\text{‰}$, from sea sulfur, it will be $+20\text{‰}$, and from sedimentary sulfur, it will be negative [73].

The S isotopes show that the $\delta^{34}S$ values of sulfide were generally less than 10‰ in the Tongling ore-cluster region, mainly concentrated in the 2‰ – 8‰ range, while the carboniferous strata of pyrite in the $\delta^{34}S$ values were 0.6‰ – 29.5‰ [74,75]. The $\delta^{34}S$ values of the Hucunnan deposit were consistent with other deposits in the area, indicating that most of the sulfur in this deposit did not originate from the strata (Figure 14), but from magma of acidic intrusive rocks in the area. Meanwhile, the $\delta^{34}S$ value of skarn ore was lower than that of porphyry ore, indicating that the ore-forming hydrothermal underwent further evolution during the intrusion process and more stratigraphic materials were involved in the skarn mineralization stage.

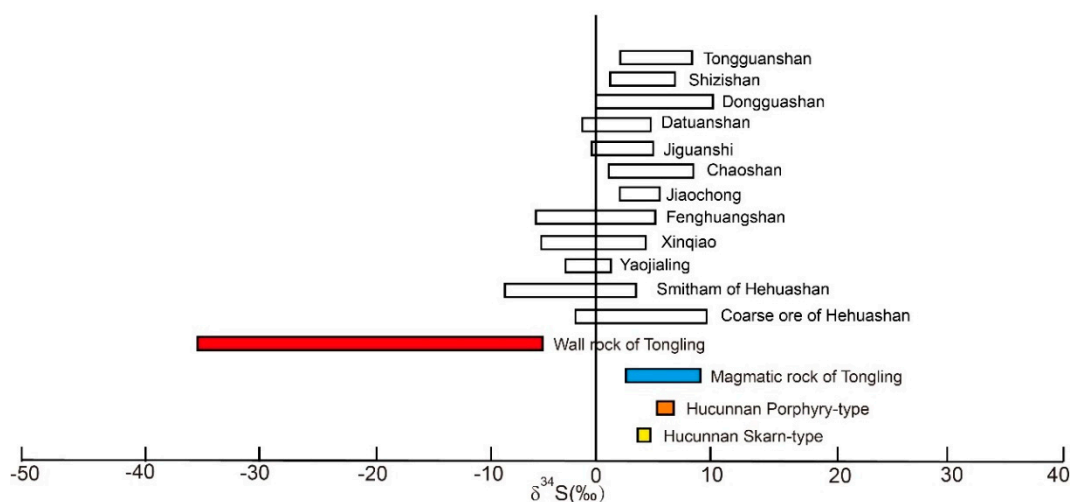


Figure 14. Distribution of sulfur isotope (data after [76–92]).

By projecting the isotopic composition of lead in various types of ore onto the diagram of $^{206}Pb/^{204}Pb$ – $^{207}Pb/^{204}Pb$, and $^{206}Pb/^{204}Pb$ – $^{208}Pb/^{204}Pb$ (Figure 15a), it can be seen that the projection

points of the isotopic composition of lead in two types of ore are relatively concentrated, suggesting that they may have had the same origin or evolutionary process [93]. The Pb isotope is located between the upper crust and the mantle. It is inferred that Pb in the Hucunnan deposit is mainly mantle-derived, which may be contaminated by crustal material (Figure 15b).

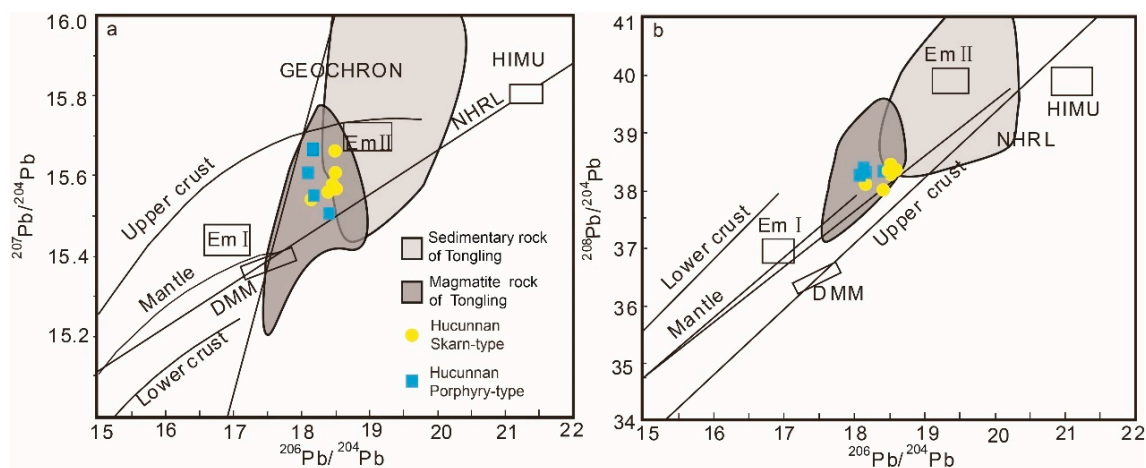


Figure 15. Pb isotope of the Tongling ore-cluster region [28]: (a) $^{207}\text{Pb}/^{204}\text{Pb}$ – $^{206}\text{Pb}/^{204}\text{Pb}$; (b) $^{208}\text{Pb}/^{204}\text{Pb}$ – $^{206}\text{Pb}/^{204}\text{Pb}$. DMM, depleted mantle component; EM I and II, enriched mantle components [94]; Geochron, zero isochron line; NHRL, northern hemisphere reference line [95]. Lines of mantle, lower crust, and upper crust of China are after [96].

The $^{206}\text{Pb}/^{204}\text{Pb}$ values of ore lead in the Hucunnan deposit were 18.10–18.54, with an average value of 18.35, which is comparable to the $^{206}\text{Pb}/^{204}\text{Pb}$ value of rock lead in the Yanshan period (18.30) and the value of post-magmatic hydrothermal deposits in the Middle and Lower Yangtze River [97,98], showing that the ore-forming materials were originated from magma. In the diagram of Pb isotope of ore, the ore sample point of Hucunnan deposit also mainly falls in the magmatic area, and a small amount of skarn ore falls in the boundary area between sedimentary and magmatic rock, which shows that ore-forming materials have the characteristics of magma source, and some stratigraphic materials were added in the skarn stage.

In conclusion, we believe that the formation of the Hucunnan Cu–Mo deposit was closely related to the intrusion of granodiorite. The ore-forming materials were mainly from magma and partly from strata. The skarn orebody has more stratigraphic materials than the porphyry orebody.

6.4. Metallogenic Geological Background

According to previous studies, during the Late Jurassic period (165 ± 5 Ma to 145 Ma), the ancient Pacific plate began to subduct, resulting in the eastern part of China being extruded and uplifted as a whole to form a plateau, suffering from erosion and missing the deposition of the Late Jurassic, and the lithosphere rapidly thickened [99,100]. A fluid or melt formed by the dehydration of the oceanic crust produced metasomatism of the mantle wedge to a low degree of partial melting of the mantle wedge or mixing with mantle magma to form alkaline basaltic magma. Then, it entered the post-collisional orogenic stress transition period (145–130 Ma). The tectonic stress transitioned from compression to tension. The alkaline basaltic magma from the enriched mantle bottom invaded the lower crust, which not only caused the crust to thicken, but also caused partial melting of the crust to form a deep magma chamber, with a part of the deep magma acidic like adakite. The adakite magma mixed with the lower crust source magma, evolved, and transgressed upward, forming intrusive rocks, mainly composed of intermediate acid in the Tongling area. Later, it entered the extensional period (130–80 Ma), during which the lithosphere was desecrated and thinned, the asthenosphere underwent upwelling, and large-scale volcanic eruption occurred in the region [27]. In the tectonic discrimination

diagrams (Figure 16), the data of Hucunnan granodiorite are mostly plotted in the field of volcanic arc granite (VAG). Combined with its diagenetic age, it would have been against the dynamic background of the transformation from compression to tension.

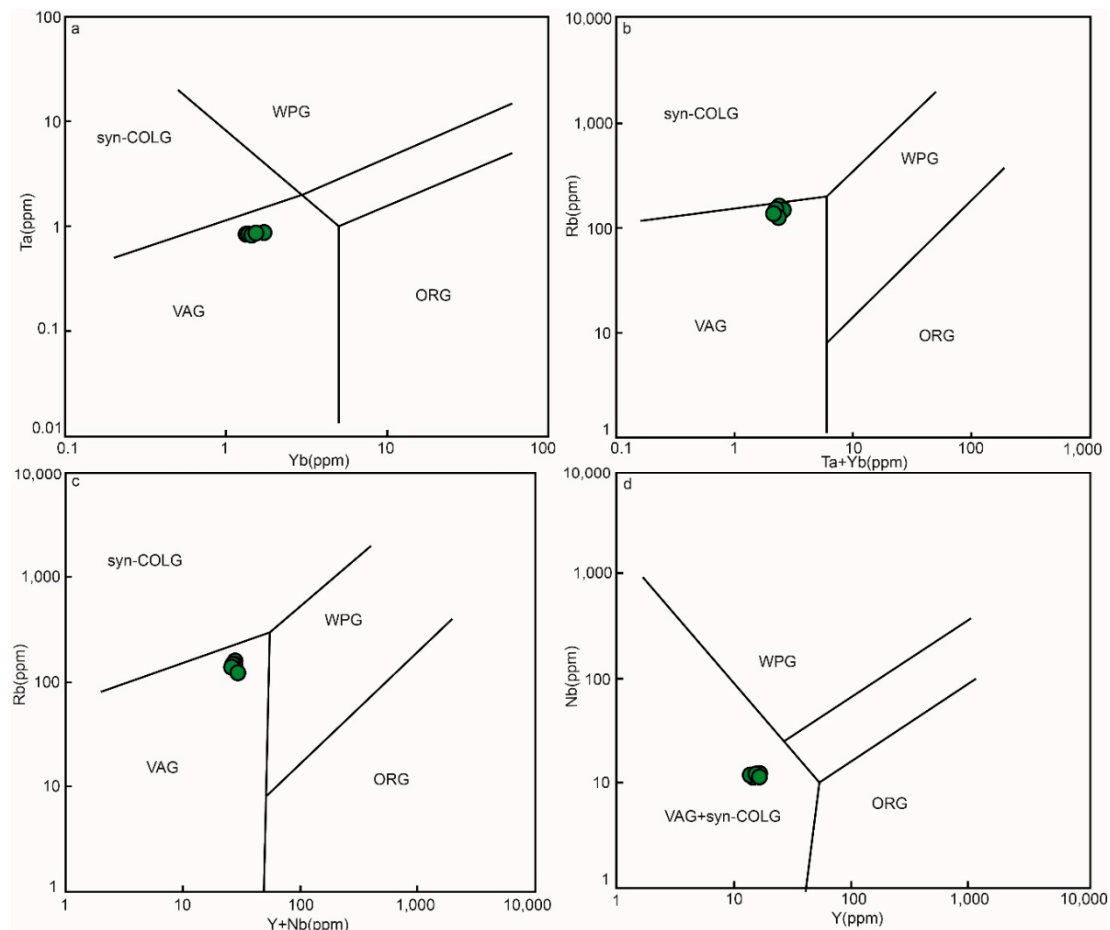


Figure 16. Tectonic discrimination of Hucunnan granodiorite: (a) Ta vs. Yb, (b) Rb vs. (Yb + Ta), (c) Nb vs. Y, and (d) Rb vs. (Y + Nb); after [101]. VAG, volcanic arc granite; ORG, oceanic ridge granite; Syn-COLG, syn-collision granite; WPG, intra-plate granite.

6.5. Metallogenic Model

According to previous studies, the diagenetic ages of granodiorite in the Tongling ore cluster are mainly from 147–137 Ma, and the metallogenic ages are mainly from 141–137 Ma [19]. The diagenetic age of Hucunnan granodiorite is 137.5 ± 1.2 Ma [36], and the ages of the metallogenic model are 138.70 ± 1.87 Ma and 140.03 ± 2.8 Ma, which are consistent with the overall diagenetic and metallogenic age of the region, indicating that magmatism and mineralization are inseparable. Research on the major elements of biotite and garnet showed that the ore-forming environment of the Hucunnan Cu–Mo deposit was characterized by high oxygen fugacity. This is consistent with the view that large-scale Cu–Mo polymetallic mineralization is closely related to high oxygen fugacity magmas [102–109]. Previous studies on the ore-forming fluid of the deposit showed that the time changes of redox conditions, acid balance, and temperature in the ore-forming fluid led to the temporal separation of copper and molybdenum in Hucunnan skarn deposit [37]. Research on the major elements and S–Pb isotopes of pyrite showed that the ore-forming materials of skarn and porphyry orebody in this deposit have similar sources. They are mainly from magma and are mixed with some stratigraphic materials. Compared with porphyry orebody, skarn orebody has more stratigraphic materials. Combined with

the geochemical characteristics of the rocks, the compositional patterns are summarized as follows (Figure 17).

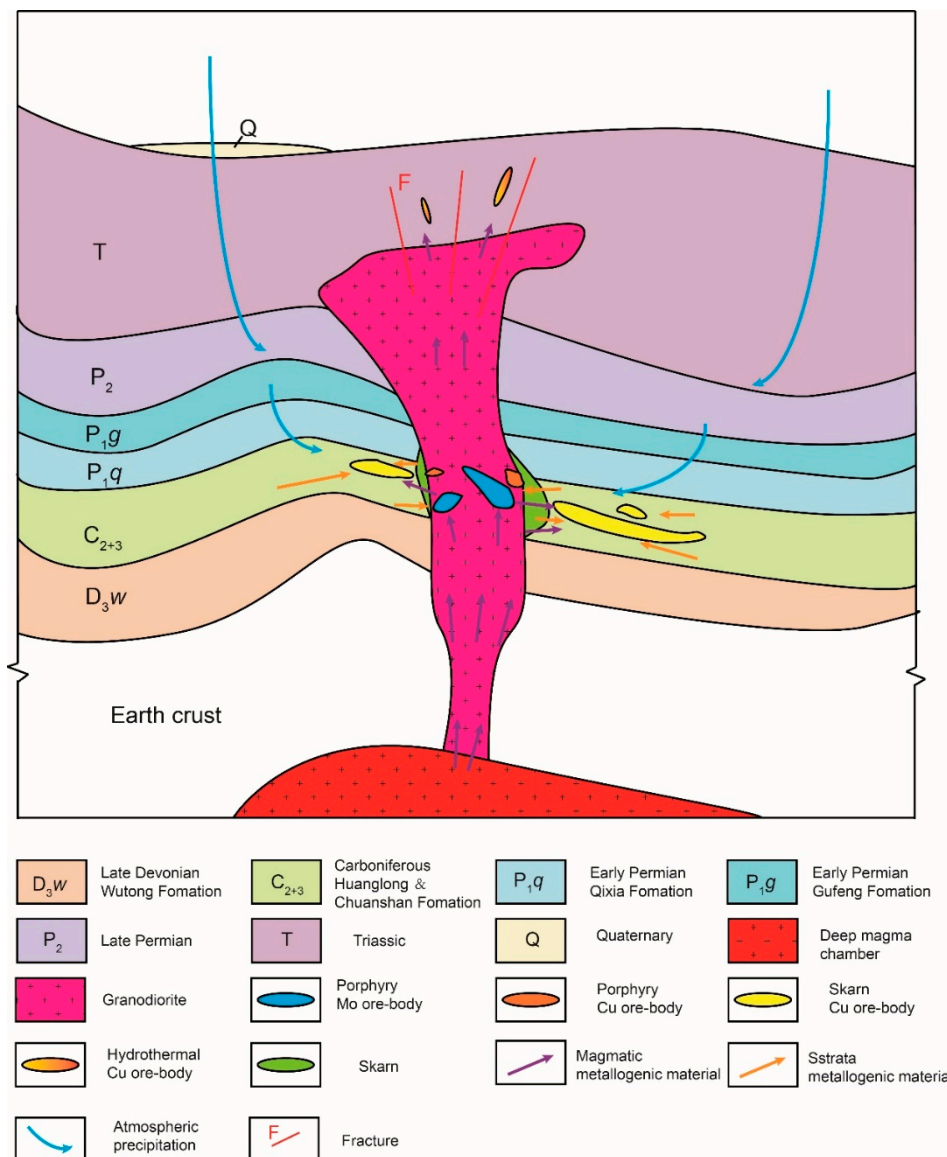


Figure 17. Metallogenic model map of the Hucunnan Cu–Mo deposit.

During 145–135 Ma, the regional tectonic stress field changed to a stress relaxation stage of transition from compression to tension. Before that, the collision and welding of the North China plate and Yangtze plate from north to south and the subsequent subduction northwest to the ancient Pacific plate resulted in lithospheric thickening and melting due to decompression. A fluid or melt formed by the dehydration of the oceanic crust made metasomatism of the mantle wedge to a low degree of partial melting of the mantle wedge or mixed with mantle magma to form alkaline basaltic magma, and the underplating of the lower crust rock formed adakitic magma. The two kinds of magma show mixed coalescence, evolution, and random rise and emplacement along the east–west deep fault. During the upwelling process, crystallization of apatite, sphene, amphibole, pyroxene, and plagioclase and assimilation and contamination of crustal materials took place, forming the Hucunnan granodiorite. Magmatism in the area not only brought ore-forming materials, but also provided a lot of heat energy for groundwater circulation. The ore-forming hydrothermal fluid rose to the shallow intrusion, forming lenticular orebodies and vein and veinlet disseminated ore in the intrusive body

and its silicate surrounding rock, developing slightly zonal K-silicified hydrothermal alteration and forming porphyry deposits. Skarnization formed in the contact zone between the rock body and carbonate formation, with strong contact thermal metamorphism. Under the influence of thermal activity and volatilization, the ore-forming materials in the strata were activated and migrated into the ore-forming hydrothermal solution, and were enriched in favorable spaces, such as interlayer fissures and fold ends, to form skarn orebodies, usually occurring along the strata. In addition, a small amount of ore-forming hydrothermal fluids continued to intrude along the fractures, forming a small-scale hydrothermal orebody near the surface, which is the end metallogenic effect of the metallogenic system.

7. Conclusions

- (1) The geochemical affinity of this granodiorite related to Cu–Mo mineralization is adakite, the metallogenic model ages of the Hucunna Cu–Mo deposit are 138.70 ± 1.87 Ma and 140.03 ± 2.8 Ma, and the ages of diagenesis and mineralization are basically the same. Magma originated in the mantle and subducted oceanic crust and mixed with some crustal material. It formed under the dynamic background of a transformation from compression to extension.
- (2) The chemical compositions of biotites show that the magma formed in a high oxygen fugacity environment, and garnets show that the ore-forming fluids in the skarn stage are characterized by high temperature, low acidity, and high oxygen fugacity.
- (3) The formation of the Hucunna Cu–Mo deposit was closely related to the intrusion of granodiorite. The ore-forming materials were mainly originated from magma and partly from strata. The skarn orebody has more stratigraphic materials than the porphyry orebody. The porphyry/skarn metallogenic system was formed under the joint action of stratum structure magmatic rocks.

Supplementary Materials: The following are available online at <http://www.mdpi.com/2075-163X/10/2/107/s1>, Table S1: Major (wt.%) and trace element (ppm) results of Hucunna granodiorites; Table S2: Chemical compositions of biotites in the Hucunna deposit; Table S3: Chemical composition of garnets in the Hucunna deposit; Table S4: Chemical composition of pyrites in the Hucunna deposit; Table S5: S isotopes of ores in the Hucunna deposit; Table S6: Pb isotopes of ores in the Hucunna deposit; Table S7: Re–Os isotopes of molybdenites in the Hucunna deposit.

Author Contributions: K.S. wrote the paper; X.Y., J.D., and J.C. designed the experiments; Q.W. and Y.C. took part in the field investigation. All authors have read and agreed to the published version of the manuscript.

Funding: This study was supported by the National Key R&D Program of China (2016YFC0600404), the Key R&D Program of Anhui Province (201904a07020077), the Natural Science Foundation of China (41673040), the Project of Geological Science and Technology of Anhui Province (2016-K-3), and the Public Welfare Projects of Anhui Province (2016-g-3-14).

Acknowledgments: The authors are grateful to three anonymous reviewers for their helpful comments and suggestions that greatly helped to improve an earlier manuscript version. We appreciate for Y. Li, K.J. Hou, and C. Duan assistance in EPMA, Re–Os isotope dating and S, Pb isotope analyses. Finally, we greatly thank L.J. Chen, S.S. Liu from No.321 Unit of Bureau of Geology and Mineral Exploration of Anhui Province for field assistance.

Conflicts of Interest: The authors declare no conflict of interest.

References

1. Atherton, M.; Petford, N. Generation of sodium-rich magmas from newly underplated basaltic crust. *Nature* **1993**, *362*, 144–146. [[CrossRef](#)]
2. Macpherson, C.; Dreher, S.; Thirwall, M. Adakites without slab melting: High pressure processing of basaltic island arc magma, Mindanao, the Philippines. *Earth Planet. Sci. Lett.* **2006**, *243*, 581–593. [[CrossRef](#)]
3. Chen, B.; Jahn, B.; Suzuki, K. Petrological and Nd–Sr–Os isotopic constraints on the origin of high-Mg adakitic rocks from the North China Craton: Tectonic implications. *Geology* **2012**, *41*, 91–94. [[CrossRef](#)]
4. Guan, N.; Zhang, Y.; Gu, X.; Peng, Y.; He, Y. Petrogenesis and mineralization of the porphyry and skarn mineralization-related Husite intrusion in the Boluokenu metallogenic belt, Western Tianshan Orogenic Belt, NW China. *J. Asian Earth Sci.* **2018**, *165*, 160–174.

5. Chen, Y.; Chen, H.; Zaw, K.; Pirajno, F.; Zhang, Z. Geodynamic settings and tectonic model of skarn gold deposits in China: An overview. *Ore Geol. Rev.* **2007**, *31*, 139–169. [[CrossRef](#)]
6. Meinert, L.; Dipple, G.; Nicolescu, S. World skarn deposits. *Econ. Geol. 100th Anniversary* **2005**, *500*, 299–336.
7. Cooke, D.; Hollings, P.; Walsh, J. Giant porphyry deposits: Characteristics, distribution, and tectonic controls. *Econ. Geol.* **2005**, *100*, 801–818. [[CrossRef](#)]
8. Sun, W.; Zhang, H.; Ling, M.; Ding, X.; Chung, S.; Zhou, J.; Yang, X.; Fan, W. The genetic association of adakites and Cu–Au ore deposits. *Int. Geol. Rev.* **2011**, *53*, 691–703. [[CrossRef](#)]
9. Gao, J.; Klemd, R.; Zhu, M.; Wang, X.; Li, J.; Wan, B.; Xiao, W.; Zeng, Q.; Shen, P.; Sun, J.; et al. Large-scale porphyry-type mineralization in the Central Asian metallogenic domain: A review. *J. Asian Earth Sci.* **2017**, *165*, 7–36. [[CrossRef](#)]
10. Imai, A. Metallogenesis of porphyry Cu deposits of the western Luzon arc, Philippines: K–Ar ages, SO₃ contents of microphenocrystic apatite and significance of intrusive rocks. *Resour. Geol.* **2002**, *52*, 147–161. [[CrossRef](#)]
11. Chang, Y.; Liu, X.; Wu, Y. *The Copper–Iron Belt of the Middle and Lower Reaches of the Changjiang River*; Beijing Geological Publishing House: Beijing, China, 1991; pp. 1–337. (In Chinese)
12. Zhai, Y.; Xiong, Y.; Yao, S.; Lin, X. Metallogeny of copper and iron deposits in the Eastern Yangtze Craton, east-central China. *Ore Geol. Rev.* **1996**, *11*, 229–248. [[CrossRef](#)]
13. Sun, W.; Xie, Z.; Chen, J.; Zhang, X.; Chai, Z.; Du, A.; Zhao, J.; Zhang, C.; Zhou, T. Os–Os Dating of copper and molybdenum deposits along the Middle and Lower Reaches of Yangtze River, China. *Econ. Geol.* **2003**, *98*, 175–180. [[CrossRef](#)]
14. Sun, W.; Ling, M.; Yang, X.; Fan, W.; Ding, X.; Liang, H. Ridge subduction and porphyry copper gold mineralization. *Sci. China Ser. D Earth Sci.* **2010**, *53*, 475–484. [[CrossRef](#)]
15. Zhou, T.; Fan, Y.; Yuan, F. Advances on petrogenesis and metallogeny study of the mineralization belt of the Middle and Lower Reaches of the Yangtze River area. *Acta Petrol. Sin.* **2008**, *24*, 1665–1678. (In Chinese with English Abstract)
16. Zhou, T.; Fan, Y.; Wang, S.; White, N. Metallogenic regularity and metallogenic model of the Middle–Lower Yangtze River Valley Metallogenic Belt. *Acta Petrol. Sin.* **2017**, *33*, 3353–3372. (In Chinese with English Abstract)
17. Xie, G.; Mao, J.; Zhu, Q.; Yao, L.; Li, Y.; Li, W.; Zhao, H. Geochemical constraints on Cu–Fe and Fe skarn deposits in the Edong district, Middle–Lower Yangtze River metallogenic belt, China. *Ore Geol. Rev.* **2015**, *64*, 425–444. [[CrossRef](#)]
18. Xie, G.; Mao, J.; Li, X.; Duan, C.; Lei, Y. Late Mesozoic bimodal volcanic rocks in the Jinniu basin, Middle–Lower Yangtze River Belt (YRB), East China: Age, petrogenesis and tectonic implications. *Lithos* **2011**, *127*, 144–164. [[CrossRef](#)]
19. Shi, K.; Du, J.; Wan, Q.; Chen, F.; Cai, Y.; Cao, J.; Wu, L.; Wang, L.; Tan, D. Chronology study of the Mesozoic intrusive rocks in the Tongling ore-cluster region, Anhui, and its metallogenic significance. *Acta Geol. Sin.* **2019**, *93*, 1096–1112. (In Chinese with English Abstract)
20. Xing, F.; Xu, X. High-potassium calc-alkaline intrusive rocks in Tongling area, Anhui Province. *Geochimica* **1996**, *25*, 29–38. (In Chinese with English Abstract)
21. Zhou, X.; Li, W. Origin of late Mesozoic igneous rocks in southeastern China, implications for lithosphere subduction and underplating of mafic magma. *Tectonophysics* **2000**, *326*, 269–278. [[CrossRef](#)]
22. Deng, J.; Wang, Q.; Huang, D.; Wan, L.; Yang, L.; Gao, B. Transport network and flow mechanism of shallow ore-bearing magma in Tongling ore cluster area. *Sci. China Ser. D* **2006**, *49*, 397–407. (In Chinese with English Abstract) [[CrossRef](#)]
23. Wu, C.; Dong, S.; Wu, D.; Zhang, X.; Ernst, W. Late Mesozoic high-K calc-alkaline magmatism in SE China: The Tongling Example. *Acta Petrol. Sin.* **2008**, *24*, 1801–1812. (In Chinese with English Abstract)
24. Wu, C.; Gao, Q.; Guo, H.; Guo, X. Petrogenesis of the intermediate-acid intrusive rocks and zircon SHRIMP dating in Tongling, Anhui, China. *Int. Geol. Rev.* **2018**, *60*, 1326–1360. [[CrossRef](#)]
25. Xie, J.; Yang, X.; Sun, W.; Du, J.; Xu, W.; Wu, L.; Wang, K.; Du, X. Geochronological and geochemical constraints on formation of the Tongling metal deposits, middle Yangtze metallogenic belt, east-central China. *Int. Geol. Rev.* **2009**, *51*, 388–421. [[CrossRef](#)]

26. Xie, J.; Yang, X.; Sun, W.; Du, J. Early Cretaceous dioritic rocks in the Tongling region, eastern China: Implications for the tectonic settings. *Lithos* **2012**, *150*, 49–61. [[CrossRef](#)]
27. Xu, X.; Bai, R.; Xie, Q.; Lou, J.; Zhang, Z.; Liu, Q.; Cheng, L. Re-understanding of the geological and geochemical characteristics of the Mesozoic intrusive rocks from Tongling area of Anhui Province, and discussions on their genesis. *Acta Petrol. Sin.* **2012**, *28*, 3139–3169. (In Chinese with English Abstract)
28. Xu, X.; Fan, Z.; He, J.; Liu, X.; Liu, X.; Xie, Q.; Lu, S.; Lou, J. Metallogenic model for the copper-gold polymetallic deposits in Shizishan ore-field, Tongling, Anhui Province. *Acta Petrol. Sin.* **2014**, *30*, 1054–1074. (In Chinese with English Abstract)
29. Fu, Z.; Xu, X.; He, J.; Fan, Z.; Xie, Q.; Du, J.; Chen, F. Genetic types and metallogenic model for the polymetallic copper-gold deposits in the Tongling ore district, Anhui Province, Eastern China. *Acta Geol. Sin.* **2019**, *93*, 88–110. [[CrossRef](#)]
30. Liu, Z.; Shao, Y.; Wang, C.; Liu, Q. Genesis of the Dongguashan skarn Cu–(Au) deposit in Tongling, Eastern China: Evidence from fluid inclusions and H–O–S–Pb isotopes. *Ore Geol. Rev.* **2019**, *104*, 462–476. [[CrossRef](#)]
31. Li, S.; Yang, X.; Huang, Y.; Sun, W. Petrogenesis and mineralization of the Fenghuangshan skarn Cu–Au deposit, Tongling ore cluster field, Lower Yangtze metallogenic belt. *Ore Geol. Rev.* **2014**, *58*, 148–162. [[CrossRef](#)]
32. Huang, X.; Gao, J.; Qi, L.; Meng, Y.; Wang, Y.; Dai, Z. In-situ LA–ICP–MS trace elements analysis of magnetite: The Fenghuangshan Cu–Fe–Au deposit, Tongling, Eastern China. *Ore Geol. Rev.* **2016**, *72*, 746–759. [[CrossRef](#)]
33. Wang, S.; Zhou, T.; Yuan, F.; Fan, Y.; White, N.; Lin, F. Geological and geochemical studies of the Shujiadian porphyry Cu deposit, Anhui Province, Eastern China: Implications for ore genesis. *J. Asian Earth Sci.* **2015**, *103*, 252–275. [[CrossRef](#)]
34. Wang, S.; Zhou, T.; Yuan, F.; Fan, Y.; Cooke, D.; Zhang, L.; Fu, B.; White, N. Geochemical characteristics of the Shujiadian Cu deposit related intrusion in Tongling: Petrogenesis and implications for the formation of porphyry Cu systems in the Middle-Lower Yangtze River Valley metallogenic belt, eastern China. *Lithos* **2016**, *252*, 185–199. [[CrossRef](#)]
35. Shi, K.; Yang, X.; Du, J.; Wan, Q.; Cai, Y.; Chen, L. Study on fluid characteristics and discussion on its metallogenic model of Yangchongli gold deposit in the Tongling, Anhui Province. *Acta Pet. Sin.* **2019**, *35*, 3734–3748. (In Chinese with English Abstract)
36. Yang, H.; Du, Y.; Lu, Y.; Cheng, L.; Zheng, Z.; Zhang, Y. U–Pb and Re–Os Geochronology of the Hucunna Copper–Molybdenum Deposit in Anhui Province, Southeast China, and its Geological Implications. *Resour. Geol.* **2016**, *66*, 303–312. [[CrossRef](#)]
37. Cao, Y.; Zheng, Z.; Du, Y.; Gao, F.; Qin, X.; Yang, H.; Lu, Y.; Du, Y. Ore geology and fluid inclusions of the Hucunna deposit, Tongling, Eastern China: Implications for the separation of copper and molybdenum in skarn deposits. *Ore Geol. Rev.* **2017**, *81*, 925–939. [[CrossRef](#)]
38. Large, R.; Danyushevsky, L.; Hollit, C.; Maslennikov, V.; Meffre, S.; Gilbert, S.; Bull, S.; Scott, R.; Emsbo, P.; Thomas, H.; et al. Gold and trace element zonation in pyrite using a laser imaging technique: Implications of the timing of gold in orogenic and Carlin-style sediment-hosted deposits. *Econ. Geol.* **2009**, *104*, 635–668. [[CrossRef](#)]
39. Deol, S.; Deb, M.; Large, R.; Gilbert, S. LA–ICPMS and EPMA studies of pyrite, arsenopyrite and loellingite from the Bhukia–Jagpura gold prospect, southern Rajasthan, India: Implications for ore genesis and gold remobilization. *Chem. Geol.* **2012**, *326*, 72–87. [[CrossRef](#)]
40. Yu, B.; Zeng, Q.; Frimmel, H.; Wang, Y.; Guo, W.; Sun, G.; Zhou, T.; Li, J. Genesis of the Wulong gold deposit, northeastern North China Craton: Constraints from fluid inclusions, H–O–S–Pb isotopes, and pyrite trace element concentrations. *Ore Geol. Rev.* **2018**, *102*, 313–337. [[CrossRef](#)]
41. Li, H.; Kong, H.; Zhou, Z.; Wu, Q.; Xi, X.; Ratio, J. Ore-forming material sources of the Jurassic Cu–Pb–Zn mineralization in the Qin–Hang ore belt, South China: Constraints from S–Pb isotopes. *Geochemistry.* **2019**, *79*, 280–306. [[CrossRef](#)]
42. Tang, Y.; Wu, Y.; Chu, G. *Geology of Copper–Gold Polymetallic Deposits along the Yangtze River, Anhui Province*; Beijing Geological Publishing House: Beijing, China, 1998. (In Chinese)
43. Duan, L.; Gu, H.; Yang, X. Geological and geochemical constraints on the newly discovered Yangchongli gold deposit in Tongling Region, Lower Yangtze Metallogenic Belt. *Acta Geol. Sin. (Engl. Ed.)* **2017**, *91*, 2078–2108. [[CrossRef](#)]

44. Xie, J.; Wang, Y.; Li, Q.; Yan, J.; Sun, W. Petrogenesis and metallogenic implications of Late Mesozoic intrusive rocks in the Tongling region, eastern China: A case study and perspective review. *Int. Geol. Rev.* **2018**, *60*, 1361–1380. [[CrossRef](#)]
45. No. 321 Geological Team of Bureau of Geology and Mineral Exploration of Anhui Province. *Geological Map of the Hucunna Cu–Mo Ore Deposit in Jiguanshan–Changlongshan Region. Tongling, China*; No. 321 Geological Team of Bureau of Geology and Mineral Exploration of Anhui Province: Tongling, China, 2010. (In Chinese)
46. Qu, W.; Du, A. Highly precise Re–Os dating of molybdenite by ICP–MS with carius tube sample digestion. *Rock Miner. Anal.* **2003**, *22*, 254–262. (In Chinese with English Abstract)
47. Li, C.; Qu, W.; Zhou, L.; Du, A. Rapid separation of osmium by direct distillation with carius tube. *Rock Miner. Anal.* **2010**, *29*, 14–16. (In Chinese with English Abstract)
48. Li, C.; Qu, W.; Du, A.; Sun, W. Comprehensive study on extraction of rhenium with acetone in re–Os isotopic dating. *Rock Miner. Anal.* **2009**, *28*, 233–238. (In Chinese with English Abstract)
49. Middlemost, E. Naming materials in the magma/igneous rock system. *Earth Sci. Rev.* **1994**, *37*, 215–224. [[CrossRef](#)]
50. Irvine, T.; Baragar, W. A guide to the chemical classification of the common volcanic rocks. *Can. J. Earth Sci.* **1971**, *8*, 523–548. [[CrossRef](#)]
51. Peccerillo, A.; Taylor, S. Geochemistry of Eocene calc-alkaline volcanic rocks from the Kastamonu area, northern Turkey. *Contrib. Mineral. Petrol.* **1976**, *58*, 63–81. [[CrossRef](#)]
52. Sun, S.; McDonough, W. Chemical and isotopic systematics of oceanic basalts: Implications for mantle composition and processes. *Geol. Soc., Lond. Spec. Publ.* **1989**, *42*, 313–345. [[CrossRef](#)]
53. Foster, M. *Interpretation of Composition of Trioctahedral Micas*; Geological Survey Professional Paper 354-B; United States Department of the Interior: Washington, DC, USA, 1960; pp. 1–49.
54. Albuquerque, A. Geochemistry of biotites from granitic rocks, northern Portugal. *Geochim. Cosmochim. Acta* **1973**, *37*, 1779–1802. [[CrossRef](#)]
55. Barrière, M.; Cotton, J. Biotites and associated minerals as markers of magmatic fractionation and deuteric equilibration in granites. *Contrib. Mineral. Petrol.* **1979**, *137*, 183–192. [[CrossRef](#)]
56. Noyes, H.; Wones, D.; Frey, F. A tale of two plutons: Petrographic and mineralogic constraints on the petrogenesis of the Red Lake and Eagle Peak plutons, Central Sierra Nevada, California. *J. Geol.* **1983**, *91*, 353–378. [[CrossRef](#)]
57. Wones, D. Significance of the assemblage titanite + magnetite + quartz in granitic rocks. *Am. Mineral.* **1989**, 744–749.
58. Wones, D.; Eugster, H. Stability of biotite: Experiment, theory, and application. *Am. Mineral.* **1965**, *50*, 1228–1272.
59. Zhou, Z. The origin of intrusive mass in Fengshandong, Hubei province. *Acta Petrol. Sin.* **1986**, *2*, 59–70. (In Chinese with English Abstract)
60. Defant, M.; Kepezhinskis, P. Evidence suggests slab melting in arc magmas. *EOS Trans. Am. Geophys. Union* **2001**, *82*, 65–69. [[CrossRef](#)]
61. Xie, J.; Chen, S.; Sun, W.; Yang, X. Geochemistry of Early Cretaceous adakitic rocks in Tongling region of Anhui Province: Constraints for rock-and ore-forming. *Acta Petrol. Sin.* **2012**, *28*, 3181–3196. (In Chinese with English Abstract)
62. Meinert, L.; Hedenquist, J.; Satoh, H.; Matsuhisa, Y. Formation of anhydrous and hydrous skarn in Cu–Au ore deposits by magmatic fluids. *Econ. Geol.* **2003**, *98*, 147–156. [[CrossRef](#)]
63. Chen, L.; Qin, K.; Li, G.; Li, J.; Xiao, B.; Jiang, H.; Zhao, J.; Fan, X.; Jiang, S. Geological and skarn mineral characteristics of Nuri Cu–W–Mo deposit in southeast Gangdese, Tibet. *Miner. Depos.* **2012**, *31*, 417–437. (In Chinese with English Abstract)
64. Zhao, J.; Newberry, R.J. Novel knowledge on the origin and mineralization of skarns from Shizhuyuan. *Acta Mineral. Sin.* **1996**, *16*, 442–449. (In Chinese with English Abstract)
65. Meinert, L. Skarn and skarn deposit. *Geosci. Can.* **1992**, *19*, 145–462.
66. Calagari, A.; Hosseinzadeh, G. The mineralogy of copper-bearing skarn to the east of the Sungun–Chay river, East-Azarbaidjan, Iran. *J. Asian Earth Sci.* **2006**, *28*, 423–438. [[CrossRef](#)]
67. Zhao, B.; Li, T.; Li, Z. Experimental study of physico-chemical condition the formation of skarns. *Geochimica.* **1983**, *3*, 256–267. (In Chinese with English Abstract)

68. Zhao, B.; Barton, M. Compositional characteristics of garnets and pyroxenes in contact-metasomatic skarn deposits and their relationship to metallization. *Acta Mineral. Sin.* **1987**, *7*, 3–8. (In Chinese with English Abstract)
69. Reich, M.; Kesler, S.; Utsunomiya, S.; Palenik, C.; Chryssoulis, S.; Ewing, R. Solubility of gold in arsenian pyrite. *Geochim. Cosmochim. Acta* **2005**, *69*, 2781–2796. [[CrossRef](#)]
70. Deditius, A.; Utsunomiya, S.; Reich, M.; Kesler, S.; Ewing, R.; Hough, R.; Walshe, J. Trace metal nanoparticles in pyrite. *Ore Geol. Rev.* **2011**, *42*, 32–46. [[CrossRef](#)]
71. Pacevski, A.; Libowitzky, E.; Zivkovic, P.; Dimitrijevic, R.; Cvetkovic, L. Copper-bearing pyrite from the Coka Marin polymetallic deposit, Serbia: Mineral inclusions or true solid-solution? *Can. Mineral.* **2008**, *46*, 249–261. [[CrossRef](#)]
72. Reich, M.; Deditius, A.; Chryssoulis, S.; Li, J.; Ma, C.; Parada, M.; Barra, F.; Mittermayr, F. Pyrite as a record of hydrothermal fluid evolution in a porphyry copper system: A SIMS/EMPA trace element study. *Geochim. Cosmochim. Acta* **2013**, *104*, 42–62. [[CrossRef](#)]
73. Chaussidon, M.; Lorand, J. Sulphur isotope composition of orogenic spinel lherzolite massifs from Ariège (North-Eastern Pyrenees, France): An ionmicroprobe study. *Geochim. Cosmochim. Acta* **1990**, *54*, 2835–2846. [[CrossRef](#)]
74. Xu, W.; Yang, Z.; Meng, Y.; Zeng, P.; Shi, D.; Tian, S.; Li, H. Genetic model and dynamic migration of ore-forming fluids in carboniferous exhalation-sedimentary massive sulfide deposits of Tongling district, Anhui Province. *Miner. Depos.* **2004**, *23*, 353–364. (In Chinese with English Abstract)
75. Liu, Z.; Shao, Y.; Zhou, X.; Zhang, Y.; Zhou, G. Hydrogen, oxygen, sulfur and lead isotope composition tracing for the metallogenic material source of Dongguashan copper (gold) deposit in Tongling, Anhui Province. *Acta Petrol. Sin.* **2014**, *30*, 199–208. (In Chinese with English Abstract)
76. Huang, X.; Chu, G.; Zhou, J.; Zhang, C.; Wu, C.; Huang, H.; Wen, C.; Shi, Q. A discussion on the sources of ore-forming material and ore-bearing fluid of the Tongling area, Anhui. *Geol. Anhui* **1994**, *4*, 1–9. (In Chinese with English Abstract)
77. Wang, Z.; Zhou, T.; Zhang, H. Study on geochemistry of Cu, Au deposit in Mashan, Anhui. *J. East China Geol. Inst.* **1996**, *19*, 36–41. (In Chinese with English Abstract)
78. Xia, Y. A tentative study on the origin of ore-forming materials of Tianmashan sulfur-gold deposit. *Miner. Resour. Geol.* **1999**, *13*, 34–38. (In Chinese with English Abstract)
79. Tian, S.; Ding, T.; Yang, Z.; Meng, Y.; Zeng, P.; Wang, Y.; Wang, X.; Jiang, Z. REE and stable isotope geochemical characteristics of Chaoshan gold deposit in Tongling, Anhui province. *Miner. Depos.* **2004**, *23*, 365–374. (In Chinese with English Abstract)
80. Tian, S.; Ding, T.; Hou, Z.; Yang, Z.; Xie, Y.; Wang, Y.; Wang, X. REE and stable isotope geochemistry of the Xiaotongguanshan copper deposit, Tongling, Anhui. *Geol. China* **2005**, *4*, 80–89. (In Chinese with English Abstract)
81. Tian, S.; Hou, Z.; Yang, Z.; Ding, T.; Meng, Y.; Zeng, P.; Wang, Y.; Wang, X. REE and Stable Isotope Geochemical Characteristics of the Mashan Au–S Deposit in Tongling, Anhui Province. *Acta Geol. Sin.* **2007**, *7*, 929–938. (In Chinese with English Abstract)
82. Xu, Z.; Lu, X.; Gao, G.; Fang, C.; Wang, Y.; Yang, X.; Jiang, S.; Chen, B. Isotope geochemistry and mineralization in the Dongguashan diagenetic stratified copper deposit, Tongling Area. *Geol. Rev.* **2007**, *53*, 44–51. (In Chinese with English Abstract)
83. Shao, Y.; Zhang, Z.; Wu, C.; Li, A.; Gu, L. Genesis of the Mashan Au–Cu–S deposit, Tongling, Anhui Province. *Contrib. Geol. Miner. Resour. Res.* **2010**, *25*, 310–318. (In Chinese with English Abstract)
84. Wang, B. Geological and geochemical characters of Shujiadian copper deposit and genesis analysis. *J. Hefei Univ. Technol. (Nat. Sci.)* **2010**, *33*, 906–910. (In Chinese with English Abstract)
85. Xu, X.; Yin, T.; Lou, J.; Lu, S.; Xie, Q.; Chu, P. Origin of Dongguashan strata bound Cu–Au skarn deposit in Tongling. Constraints of sulfur isotope. *Acta Petrol. Sin.* **2010**, *26*, 2739–2750. (In Chinese with English Abstract)
86. Yang, Q.; Wang, J.; Feng, J.; Hou, Z.; Yang, Z.; Meng, Y.; Wang, C.; Chen, W. Geological and Geochemical Characteristics of the Tianmashan Au–S Deposit in Tongling, Anhui Province. *Acta Geosci. Sin.* **2010**, *31*, 203–208. (In Chinese with English Abstract)
87. Qu, H.; Pei, R.; Li, J.; Wang, Y. SHRIMP U–Pb dating of zircon from the Fenghuangshan quartz monzodiorite and granodiorite in Tongling area, Anhui Province and its geological implication. *J. Jilin Univ. (Earth Sci. Ed.)* **2010**, *40*, 581–590.

88. Qu, H.; Pei, R.; Wang, H.; Li, J.; Wang, Y.; Mei, Y. Mantle-derived ore-forming fluids of the Fenghuangshan Cu deposit, evidences from microthermometric and isotopic studies. *Geol. Rev.* **2011**, *57*, 50–62. (In Chinese with English Abstract)
89. Zhang, Z.; Zhang, D.; Di, Y.; Shu, B.; Pang, Z.; Du, Z.; Que, C.; Ma, X.; Xue, J. Sulfur, lead isotope composition characteristics of the Jiaochong Au–S ore deposit in Tongling area and their indication significance. *Geol. Bull. China.* **2013**, *32*, 1643–1652. (In Chinese with English Abstract)
90. Zhang, Y.; Shao, Y.; Wu, C.; Cheng, H. LA-ICP-MS trace element geochemistry of garnets: Constraints on hydrothermal fluid evolution and genesis of the Xinqiao Cu–S–Fe–Au deposit, eastern China. *Ore Geol. Rev.* **2017**, *86*, 426–439. [[CrossRef](#)]
91. Zhang, Y.; Shao, Y.; Li, H.; Liu, Z. Genesis of the Xinqiao Cu–S–Fe–Au deposit in the Middle–Lower Yangtze River Valley metallogenic belt, Eastern China: Constraints from U–Pb–Hf, Rb–Sr, S, and Pb isotopes. *Ore Geol. Rev.* **2017**, *86*, 100–116. [[CrossRef](#)]
92. Liu, G.; Yuan, F.; Deng, Y.; Jowitt, S.; Sun, W.; White, N.; Ynang, D.; Li, X.; Zhou, T.; Huizenga, J. The genesis of the Hehuashan Pb–Zn deposit and implications for the Pb–Zn prospectivity of the Tongling district, Middle–Lower Yangtze River Metallogenic Belt, Anhui Province, China. *Ore Geol. Rev.* **2018**, *101*, 105–112. [[CrossRef](#)]
93. Liang, T.; Wang, D.; Cai, M.; Cehn, Z.; Guo, C.; Huang, H. Sulfur and Lead Isotope Composition Tracing for the Sources of Ore-Forming Material in Dachang Tin-Polymetallic Orefield, Guangxi. *Acta Geol. Sin.* **2008**, *7*, 967–977. (In Chinese with English Abstract)
94. Zindler, A.; Hart, S. Chemical geodynamics. *Annu. Rev. Earth Planet. Sci.* **1986**, *14*, 493–571. [[CrossRef](#)]
95. Hart, S.R. A large scale isotope anomaly in the Southern Hemisphere mantle. *Nature* **1984**, *309*, 753–757. [[CrossRef](#)]
96. Li, L.; Zhen, Y.; Zhou, J. Dynamic model for Pb isotope evolution in the continental crust of China. *Acta Petrol. Sin.* **2001**, *17*, 61–68. (In Chinese with English Abstract)
97. Wang, D.; Fu, D.; Wu, L. A discussion of the middle- carboniferous “sedimentary-submarine effusive sedimentary-hydrothermal reformation” bedded Cu (Fe, S, Au, Pb, Zn, Ag) ore deposits in the Lower Yangtze Area. *East China Geol.* **1987**, *2*, 119–128. (In Chinese with English Abstract)
98. Yu, C.; Yuan, X. The relationship between mineralization and evolution of rock in Tongshan Guichi. *Miner. Resour. Geol.* **1999**, *5*, 274–278. (In Chinese with English Abstract)
99. Dong, S.; Qiu, R. *Tectonism and Magmatism of Yueshan Area in Anqing*; Beijing Geological Publishing House: Beijing, China, 1993; pp. 1–158. (In Chinese)
100. Zhang, Q.; Wang, Y.; Wang, Y. Preliminary study on the components of the lower crust in East China Plateau during Yanshanian Period: Constraints on Sr and Nd isotopic compositions of adakite-like rocks. *Acta Petrol. Sin.* **2001**, *17*, 505–513. (In Chinese with English Abstract)
101. Pearce, J.; Harris, N.; Tindle, A. Trace element discrimination diagrams for the tectonic interpretation of granitic rocks. *J. Petrol.* **1984**, *25*, 956–983. [[CrossRef](#)]
102. Sun, W.; Liang, H.; Ling, M.; Zhan, M.; Ding, X.; Zhang, H.; Yang, X.; Li, Y.; Ireland, T.; Wei, Q. The link between reduced porphyry copper deposits and oxidized magmas. *Geochim. Cosmochim. Acta* **2013**, *103*, 263–275. [[CrossRef](#)]
103. Sun, W.; Huang, R.; Li, H.; Hu, Y.; Zhang, C.; Sun, S.; Zhang, L.; Ding, X.; Li, C.; Zartman, R. Porphyry deposits and oxidized magmas. *Ore Geol. Rev.* **2015**, *65*, 97–131. [[CrossRef](#)]
104. Sun, W.; Wang, J.; Zhang, L.; Zhang, C.; Li, H.; Ling, M.; Ding, X.; Li, C.; Liang, H. The formation of porphyry copper deposits. *Acta Geochim.* **2017**, *36*, 9–15. [[CrossRef](#)]
105. Deng, J.; Yang, X.; Li, S.; Gu, H.; Mastoi, A.S.; Sun, W. Partial melting of subducted paleo-Pacific plate during the early Cretaceous: Constraint from adakitic rocks in the Shaxi porphyry Cu–Au deposit, Lower Yangtze River Belt. *Lithos* **2016**, *262*, 651–667. [[CrossRef](#)]
106. Zhang, C.; Sun, W.; Wang, J.; Zhang, L.; Sun, S.; Wu, K. Oxygen fugacity and porphyry mineralization: A zircon perspective of Dexing porphyry Cu deposit, China. *Geochim. Cosmochim. Acta* **2017**, *206*, 343–363. [[CrossRef](#)]
107. Gu, H.; Yang, X.; Nie, Z.; Deng, J.; Duan, L.; Hu, Q.; Shakoor, M.; Gao, E.; Hafiz, A. Study of Late-Mesozoic magmatic rocks and their related copper-gold-polymetallic deposits in the Guichi ore-cluster district, Lower Yangtze River Metallogenic Belt, East China. *Int. Geol. Rev.* **2018**, *60*, 1404–1434. [[CrossRef](#)]

108. Hu, Z.L.; Yang, X.Y.; Lee, I.S. Geochemical study of Cretaceous magmatic rocks in Chuzhou region, Low Yangtze River Metallogenic Belt: Implications for petrogenesis and Cu–Au mineralization. *Int. Geol. Rev.* **2018**, *60*, 1479–1506. [[CrossRef](#)]
109. Liu, Z.; Yang, X.Y.; Liu, C.M.; Huang, D.Z.; Zhou, W.J.; Teng, X.; Liang, E.Y.; Dai, T.G. Genesis of Early Cretaceous porphyrite-type iron deposits and related sub-volcanic rocks in the Ningwu Volcanic Basin, Middle-Lower Yangtze Metallogenic Belt, SE China. *Int. Geol. Rev.* **2018**, *60*, 1507–1528. [[CrossRef](#)]



© 2020 by the authors. Licensee MDPI, Basel, Switzerland. This article is an open access article distributed under the terms and conditions of the Creative Commons Attribution (CC BY) license (<http://creativecommons.org/licenses/by/4.0/>).